AGU PUBLICATIONS

JGR

Journal of Geophysical Research: Earth Surface

RESEARCH ARTICLE

10.1002/2016JF003933

Key Points:
- Debris flow runup is influenced by both smooth momentum fluxes and abrupt momentum jumps
- Runup heights vary systematically with slope angle, effective basal friction, and flow Froude number
- Accurate runup predictions must account for the unsteadiness of incoming flows

Supporting Information:
- Supporting Information S1
- Data Set S1
- Data Set S2
- Data Set S3
- Data Set S4
- Movie S1
- Movie S2
- Movie S3
- Movie S4
- Movie S5
- Movie S6
- Movie S7
- Movie S8

Correspondence to:
R. M. Iverson,
riverson@usgs.gov

Citation:
Iverson, R. M., D. L. George, and M. Logan (2016), Debris flow runup on vertical barriers and adverse slopes, *J. Geophys. Res. Earth Surf.*, *121*, 2333–2357, doi:10.1002/2016JF003933.

Received 22 APR 2016
Accepted 14 NOV 2016
Accepted article online 16 NOV 2016
Published online 13 DEC 2016

Published 2016. This article is a US Government work and is in the public domain in the United States of America.

Debris flow runup on vertical barriers and adverse slopes

Richard M. Iverson[1], David L. George[1], and Matthew Logan[1]

[1]U.S. Geological Survey, Vancouver, Washington, USA

Abstract Runup of debris flows against obstacles in their paths is a complex process that involves profound flow deceleration and redirection. We investigate the dynamics and predictability of runup by comparing results from large-scale laboratory experiments, four simple analytical models, and a depth-integrated numerical model (D-Claw). The experiments and numerical simulations reveal the important influence of unsteady, multidimensional flow on runup, and the analytical models highlight key aspects of the underlying physics. Runup against a vertical barrier normal to the flow path is dominated by rapid development of a shock, or jump in flow height, associated with abrupt deceleration of the flow front. By contrast, runup on sloping obstacles is initially dominated by a smooth flux of mass and momentum from the flow body to the flow front, which precedes shock development and commonly increases the runup height. D-Claw simulations that account for the emergence of shocks show that predicted runup heights vary systematically with the adverse slope angle and also with the Froude number and degree of liquefaction (or effective basal friction) of incoming flows. They additionally clarify the strengths and limitations of simplified analytical models. Numerical simulations based on a priori knowledge of the evolving dynamics of incoming flows yield quite accurate runup predictions. Less predictive accuracy is attained in ab initio simulations that compute runup based solely on knowledge of static debris properties in a distant debris flow source area. Nevertheless, the paucity of inputs required in ab initio simulations enhances their prospective value in runup forecasting.

1. Introduction

Runup of debris flows against obstacles in their paths is a central problem in debris flow mechanics. Runup behavior provides a stringent test of physically based debris flow models because it involves a combination of flow deceleration and redirection that challenges the ability of models to conserve mass and momentum accurately. Prediction of runup also has great practical relevance, because runup can cause overtopping and damage of protective barriers or other manmade structures in debris flow paths [e.g., *Hungr et al*., 1984, 1987]. Furthermore, geological deposits and trim lines produced during runup may provide useful ex post facto estimates of debris flow speeds [e.g., *Pierson*, 1985]—but only if models that relate flow speeds to runup heights are well-founded (Figure 1). Runup can additionally generate strong long-period seismic signals that facilitate estimation of the timing and size of remotely detected debris flows [e.g., *Allstadt*, 2013]. Interpretation of signal amplitudes rests on physical understanding of runup dynamics. Improved understanding of these dynamics can also aid interpretation and prediction of runup caused by other ground-hugging geophysical mass flows, such as wet snow avalanches, rock avalanches, dam-break water floods, and dense pyroclastic flows [e.g., *Jóhannesson et al*., 2009; *Mancarella and Hungr*, 2010; *George*, 2010; *Loughlin et al*., 2002].

Here we use several methods to evaluate the dynamics and predictability of debris flow runup. We first present alternative analytical models derived to predict the maximum runup heights produced by steady incoming flows. These models are necessarily simplistic, but they are important because they help frame key physical concepts that are essential for understanding runup behavior. We next present observations and data from four large-scale experiments that involved runup of realistic, unsteady debris flows on vertical barriers and adverse slopes. To quantify our interpretation of the complicated dynamics evident in the experiments, we first use the analytical models and then use a depth-integrated, shock-capturing numerical model (D-Claw) to predict the measured runup heights. The numerical predictions—as well as some of the analytical predictions—can be quite accurate if they are informed by a priori knowledge of the time-dependent speeds and depths of the incoming flows. We then address the more challenging problem of ab initio runup

Figure 1. Oblique aerial photograph of a 270 m high runup trimline (on left) produced by a ~50×10^6 m^3 debris flow at Mount Meager, British Columbia, Canada, on 6 August 2010 (see *Guthrie et al.* [2012] and *Allstadt* [2013] for details). Red arrow in inset image at lower right shows the orientation of the large photo, which was taken near a T confluence where Capricorn Creek discharges into Meager Creek at 50.606°N/123.430°W. Photo courtesy of Dave Steers.

prediction, in which the evolving speeds and depths of incoming flows are unspecified and are instead computed as part of numerical solutions. Comparison of the ab initio predictions with the experimental data shows that D-Claw provides a useful but inexact tool for runup forecasting. Finally, to recapitulate the relationships among various runup models, we compare runup heights predicted by the analytical models with those predicted by numerical simulations that employ the same steady inflow assumptions that are used in deriving the analytical models. The comparison shows why different methods of runup prediction can yield consistent results in some circumstances and disparate results in others.

2. Analytical Models of Runup

Alternative analytical models of runup share some important common features, but they arise from different conceptualizations of runup mechanics (Figure 2). The four analytical models we consider each assume that the flow impinging on an obstacle is homogeneous, steady, uniform, one-dimensional (1-D), and unaffected

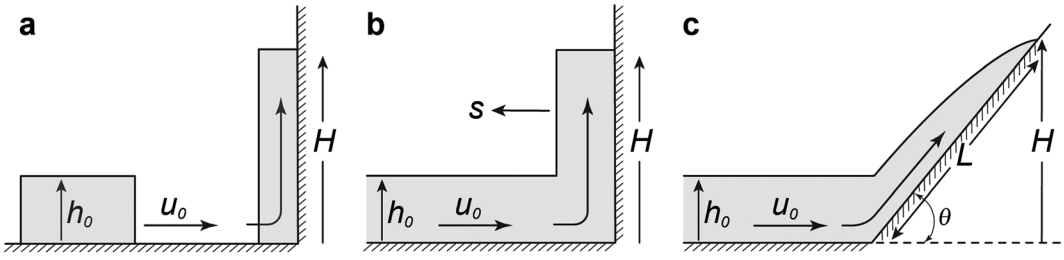

Figure 2. Schematic vertical cross sections illustrating alternative analytical models of runup. (a) Finite mass (FM) model; (b) momentum jump (MJ) model; (c) smooth momentum flux (SMF) model. In Figure 2b, *s* is the speed of a shock that migrates upstream.

by the dynamics of runup on the obstacle. Thus, the incoming flow must be supercritical, for otherwise the assumption of steady, uniform inflow would be violated as backwater effects develop. If a subcritical flow encounters an obstacle, then the maximum runup height may be determined largely by the progressive accumulation of mass behind the obstacle rather than by the dynamics of runup [cf. *Jóhannesson et al*., 2009; *Armanini et al*., 2011].

The first two analytical models treat a debris flow as a highly idealized frictionless point mass or finite mass, respectively, whereas the other two models are based on 1-D, depth-integrated continuum mechanical equations that describe simultaneous transfer of mass and momentum from the flow body to the flow head during runup. One of these continuum models assumes that a momentum jump (or shock) occurs during this transfer, and the other assumes that the transfer is smooth. In the jump model, all energy dissipation occurs within the shock, whereas the smooth transfer model assumes that all energy dissipation is caused by basal friction. Despite the significant effects of energy dissipation, each continuum model can in some cases predict runup heights that exceed those predicted by the frictionless mass models—owing to the effects of continuous momentum transfer from the flow body to the flow head.

2.1. Frictionless Point Mass (PM) Model

The well-known point mass (PM) model considers the behavior of an infinitesimal rigid body with mass m and approach speed u_0 that coverts all of its initial kinetic energy $(1/2)mu_0^2$ to gravitational potential energy mgH when it encounters an obstacle and ascends a vertical distance H. Equating the initial kinetic and final potential energies of the point mass then yields a runup formula that is typically expressed as $H = u_0^2/2g$, where g is the magnitude of gravitational acceleration. Here to facilitate comparisons with other runup formulas, it is useful to write the PM formula in the dimensionless form

$$\frac{H}{u_0^2/g} = \frac{1}{2}. \tag{1}$$

This formula has commonly been used to estimate flow speeds from runup heights [e.g., *Jibson et al*., 2006], but it neglects many important aspects of runup behavior.

2.2. Frictionless Finite Mass (FM) Model

A more complete runup model for a frictionless body can be obtained by considering a mechanical energy balance for a finite mass (FM) of fixed bulk density. The mass has a vertical thickness h_0 and depth-averaged speed u_0 as it approaches an obstacle (Figure 2a), implying that the body's center of mass has gravitational potential energy $(1/2)gh_0$, kinetic energy $(1/2)u_0^2$, and total mechanical energy $(1/2)[gh_0 + u_0^2]$ per unit mass. During runup to a maximum height H, this total energy is converted to center-of-mass potential energy, which is $(1/2)gH$ per unit mass. Equating $(1/2)[gh_0 + u_0^2]$ and $(1/2)gH$ then yields a runup formula that can be expressed as

$$\frac{H}{u_0^2/g} = 1 + \frac{1}{\mathrm{Fr}_0^2}, \tag{2}$$

where $\mathrm{Fr}_0 = u_0/\sqrt{gh_0}$ is the Froude number of the incoming flow. By using the relationship $H/h_0 = [H/(u_0^2/g)]\,\mathrm{Fr}_0^2$, (2) can be expressed in the alternative form $H/h_0 = 1 + \mathrm{Fr}_0^2$. This equation as well as (2) predict runup heights that universally exceed those predicted by the point mass formula (1) (Figures 3a and 3b).

2.3. Momentum Jump (MJ) Model

A more rigorous approach for obtaining a runup formula considers an abrupt change in macroscopic momentum (i.e., a shock or jump) that develops if a continuous, steady, uniform flow encounters a stationary obstacle that forces the flow front velocity to decelerate from u_0 to 0. The consequent conversion of macroscopic momentum to internal pressure is accompanied by an abrupt upward jump in the flow's surface elevation. The flow's surface elevation downstream of the jump determines the runup height (Figure 2b). The momentum jump (MJ) approach has its greatest relevance for cases in which a barrier oriented normal to the flow path forces a complete stoppage of downstream flow.

A runup formula obtained by using the MJ approach was presented by *Hákonardóttir et al*. [2003] and *Jóhannesson et al*. [2009], whose work focused on snow avalanches, and was again reported (but with an

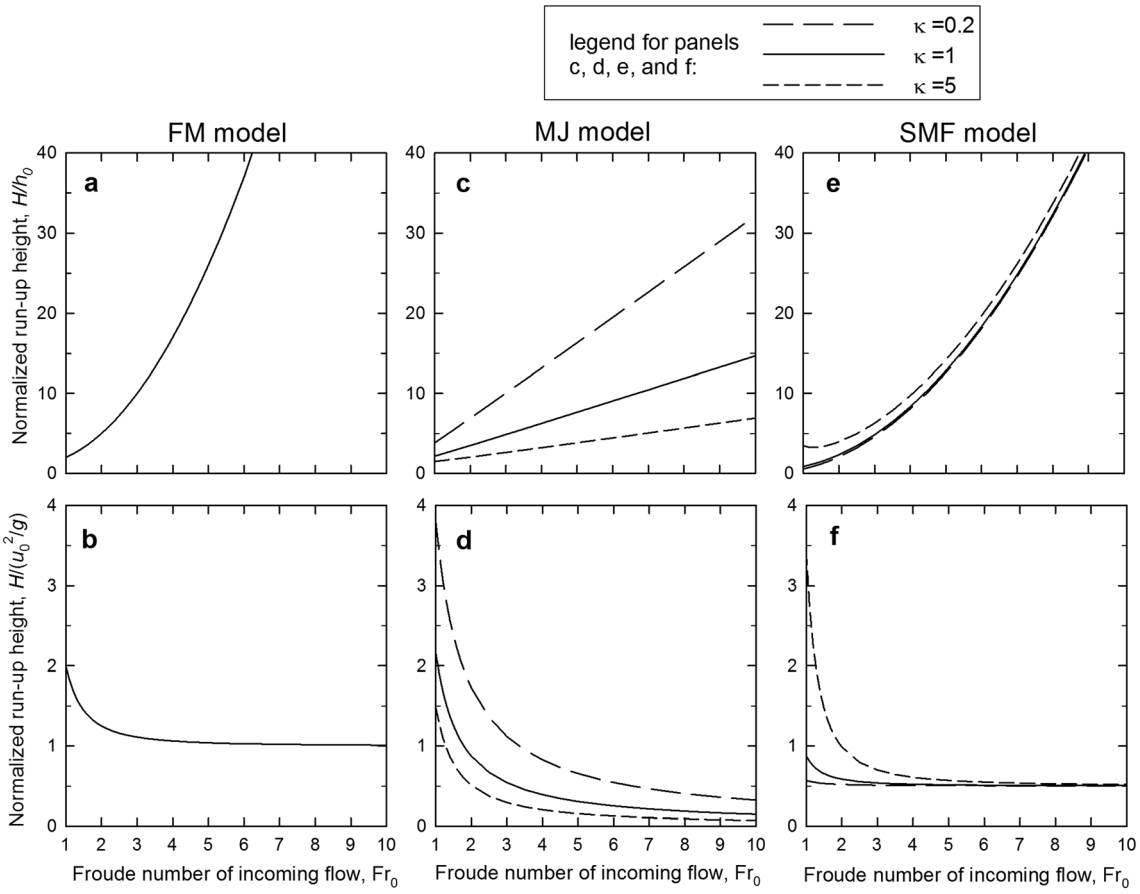

Figure 3. Graphs of normalized runup heights H/h_0 and $H/({u_0}^2/g)$ predicted by three analytical models. (a and b) Finite mass (FM) model. (c and d) Momentum jump (MJ) model. (e and f) Smooth momentum flux (SMF) model for cases with $\phi_e = \theta = 30°$. As indicated in the legend, predictions of the MJ and SMF models depend on the value of the longitudinal pressure coefficient, κ, which equals 1 if pressures are isotropic and exceeds 1 if the longitudinal pressure surpasses the bed-normal pressure.

typographical error) by *Choi et al*. [2015]. In Appendix A we derive a generalized version of the formula, which accounts for the possibility of nonhydrostatic longitudinal normal stresses. The derivation also accounts for the possibility that the jump in flow height may be accompanied by a jump in flow bulk density from ρ_0 upstream of the jump to ρ_1 downstream of the jump. For the special case in which $\rho_0 = \rho_1$ applies, the MJ formula in Appendix A reduces to

$$\frac{H}{{u_0}^2/g} = \frac{2}{\kappa}\left(\frac{H/h_0}{(H/h_0)^2 - 1}\right) + \frac{1}{{\mathrm{Fr}_0}^2}, \tag{3}$$

where the pressure coefficient κ describes the ratio of longitudinal to vertical normal stress. The value $\kappa = 1$ applies if normal stresses are isotropic, but the full-scale range of plausible κ values for typical frictional debris is roughly 0.2 to 5, depending on whether deformation occurs in an extensional or compressional mode [cf. *Iverson and Denlinger*, 2001]. Importantly, (3) can be rearranged to obtain an equation in which H/h_0 is the only dependent variable by using the relationship $H/h_0 = [H/({u_0}^2/g)]{\mathrm{Fr}_0}^2$.

By recasting (3) as a cubic equation for H/h_0 and then finding the physically relevant root of that equation (Appendix A), we construct graphs that illustrate how the predicted normalized runup heights H/h_0 and $H/({u_0}^2/g)$ vary as functions of Fr_0 and κ (Figures 3c and 3d). The graphs show that as the value of Fr_0 increases, the predicted value of H/h_0 increases (Figure 3c), whereas the predicted runup gauged by $H/({u_0}^2/g)$ decreases (Figure 3d). These trends are qualitatively similar to those predicted by the FM model (Figures 3a and 3b), but they illustrate the quantitative effects of continuous momentum inflow as well as energy dissipation within the jump.

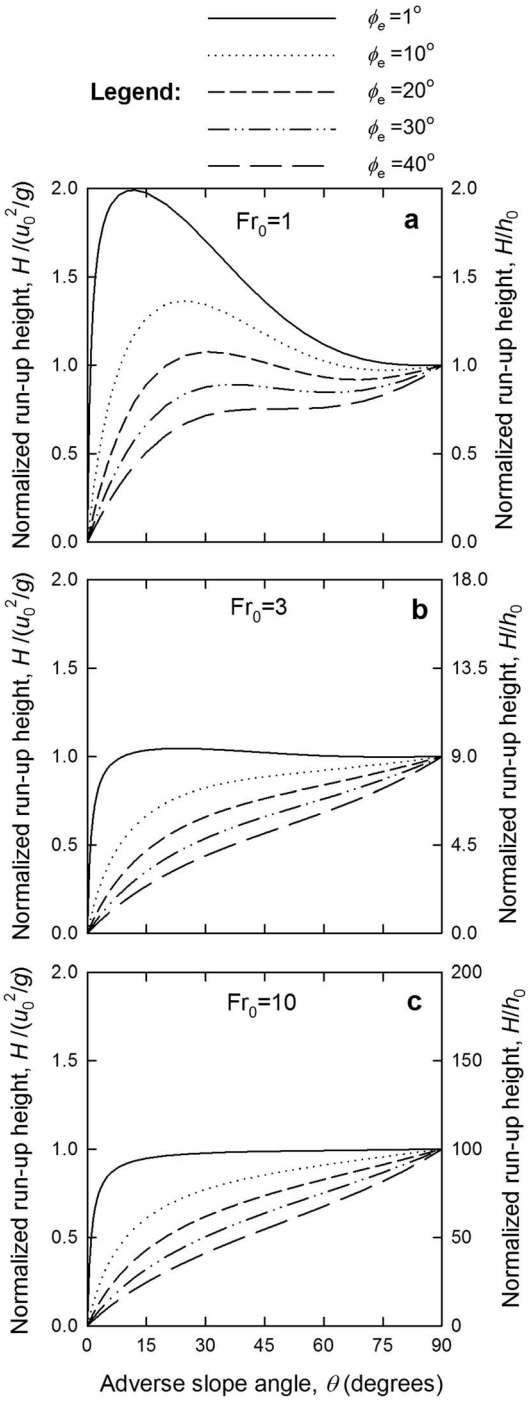

Figure 4. Normalized runup heights predicted by the smooth momentum flux (SMF) model for cases with a range of ϕ_e, θ, and Fr_0 values and a fixed value $\kappa = 1$. Panels a–c use a consistent scale for $H/(u_0^2/g)$ but use a scale for H/h_0 that expands in proportion to Fr_0^2.

2.4. Smooth Momentum Flux (SMF) Model

A different approach for calculating runup height considers a smooth transfer of mass and momentum from the flow body to the flow head during runup on an adverse slope (Figure 2c). The resulting SMF formula predicts the maximum runup height attained when a steady momentum flux into the head is balanced by steady resistive forces due to the head's basal friction and weight. This approach, originally outlined by *Takahashi and Yoshida* [1979] and articulated further by *Hungr and McClung* [1987], *Chu et al.* [1995], and *Mancarella and Hungr* [2010], considers gradual deceleration of the head rather than the abrupt deceleration associated with a momentum jump. In Appendix B we use this approach to derive an SMF runup formula that is appropriate if all incoming flow momentum is transferred upslope and all basal resistance is caused by effective Coulomb friction, which implicitly accounts for any friction reduction by pore fluid pressure. The formula in Appendix B also accounts for the possibility that the bulk density of the incoming flow may differ from that of the flow on the adverse slope, but for the special case in which these bulk densities are equal, it reduces to

$$\frac{H}{u_0^2/g} = \frac{\left(1 + \frac{\kappa}{2}\frac{\cos^3\theta}{Fr_0^2}\right)^2}{1 + \frac{\tan\phi_e}{\tan\theta}}, \qquad (4)$$

where θ is the angle of inclination of the adverse slope and ϕ_e is the effective basal friction angle of debris on the slope. As is the case with (2) and (3), (4) can be recast as an equation with H/h_0 on the left-hand side by using the relationship $H/h_0 = [H/(u_0^2/g)]Fr_0^2$.

The presence of the parameters ϕ_e and θ in (4) makes it difficult to portray all predictions of the SMF model concisely, but some important trends can be illustrated by setting $\phi_e = \theta = 30°$ and then graphing $H/(u_0^2/g)$ and H/h_0 as functions of Fr_0 and κ (Figures 3e and 3f). These trends are broadly similar to those predicted by the FM and MJ models; they show that H/h_0 increases as Fr_0 increases, while $H/(u_0^2/g)$ decreases. However, the predictions of the SMF model generally exhibit less sensitivity to the value of κ than do the predictions

of the MJ model. Moreover, increasing the value of κ yields enhanced runup heights in the SMF model (Figures 3e and 3f) but reduced runup heights in the MJ model (Figures 3c and 3d). This difference reflects different roles of longitudinal pressure during runup. In the SMF model, increased longitudinal pressure helps push debris upslope (Appendix B), but in the MJ model, increased longitudinal pressure bolsters the effectiveness of the height jump in balancing the effect of the momentum jump (Appendix A).

The most significant trends in the behavior predicted by (4) can be illustrated by fixing the value $\kappa = 1$ and then graphing $H/(u_0^2/g)$ and H/h_0 as functions of θ and ϕ_e for several values of Fr_0 (Figure 4). The graphs show that the predicted runup height universally decreases as the effective basal friction increases, provided that Fr_0 and the adverse slope angle θ remain constant. On the other hand, the effects of variations in θ on the predicted runup height can be nonmonotonic, particularly if the values of Fr_0 and ϕ_e are relatively small (Figures 4a and 4b). These nonmonotonic trends result from the competing effects of θ on the slope-normal and slope-parallel components of the flow head's weight when relatively little basal friction is engaged. In the limiting case with $\theta = 90°$, the absence of a slope-normal weight component implies that no basal friction is engaged, and the predictions of the SMF model (4) reduce to $H/(u_0^2/g) = 1$ and $H/h_0 = \mathrm{Fr}_0^2$. These predictions converge to those of the FM model (2) for $\mathrm{Fr}_0 \gg 1$, but they stand in contrast to those of the MJ model (3), which predicts that H/h_0 grows roughly in proportion to Fr_0 while $H/(u_0^2/g)$ declines roughly in proportion to $1/\mathrm{Fr}_0$. This disparity in the models' predictions is unsurprising, because as $\theta \to 90°$, the assumptions used to derive the MJ formula (3) have increasing validity, while those used to derive the SMF formula (4) have decreasing validity (Appendix A and Appendix B).

3. Large-Scale Runup Experiments

Most debris flows differ significantly from the steady, uniform, homogenous, 1-D incoming flows that are assumed in deriving the analytical runup models summarized in section 2. Many of these differences were manifested in four large-scale experiments conducted at the U.S. Geological Survey (USGS) debris flow flume in June 1994 and May 1997. One pair of replicate experiments involved debris flow runup on a 30° adverse slope, and another pair involved runup on a vertical barrier (Figure 5). Complete video documentation of each experiment is viewable online [*Logan and Iverson*, 2007], and concise video summaries are included here as supporting information Movies S1–S4. A prominent feature visible in the video documentation is the marked unsteadiness of the incoming flows.

Each experiment began with a sudden release of about 10 m^3 of water-saturated sand and gravel from behind a vertical head gate located near the top of the flume, about 90 m from the runup obstacles (Table 1). The resulting flows were "SG Smooth Bed" debris flows like those documented by *Iverson et al*. [2010], who provided details of the flume geometry, initial and boundary conditions, material properties, and experiment protocols used to generate the flows. The permanent sidewalls of the 2 m wide flume terminate at $x = 82.4$ m (where x is a longitudinal coordinate that originates at the head gate and parallels the flume bed), but in the runup experiments reported here, the sidewalls were extended several meters by placing vertical concrete panels on the runout surface at the foot of the flume (Table 1). The panels channelized the debris flows and helped them maintain high speeds as they crossed the nearly horizontal runout surface and encountered obstacles.

3.1. Flow Behavior Prior to Runup

As the experimental debris flows descended the flume, their gross behavior was quite reproducible. The chief attributes of this behavior were summarized in the aggregated SG smooth bed data set presented by *Iverson et al*. [2010]. The flows accelerated and elongated between $x = 0$ and $x = 74$ m, where the flume bed uniformly sloped 31°. When flow fronts reached a measurement cross section at $x \approx 66$ m, their maximum depths were about 0.1 m and speeds were about 15 m/s. These high speeds were promoted by the smooth flume bed and by widespread sediment liquefaction caused by high pore fluid pressures that developed as the loosely packed wet debris was released from behind the head gate. As downslope motion proceeded, frictional resistance became highest at debris flow fronts, where grain size segregation produced gravel-rich snouts that lacked much pore fluid pressure [cf. *Iverson*, 1997; *Major and Iverson*, 1999; *Johnson et al*., 2012].

In each experiment resistive, gravel-rich snouts also developed at the fronts of secondary waves, which formed spontaneously and resembled roll waves that develop in open-channel flows of liquid at high

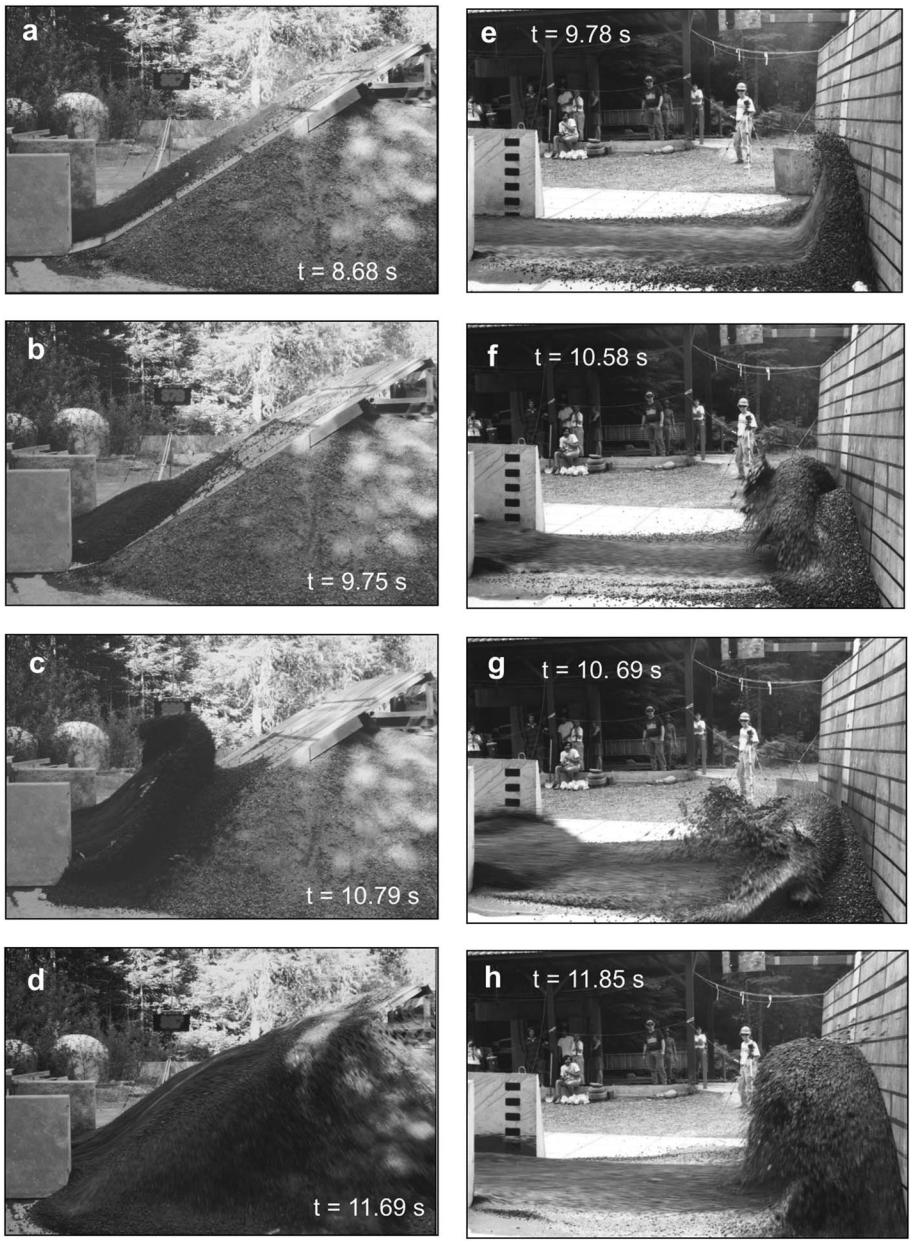

Figure 5. Sequences of stop-action photographs of two large-scale experimental debris flows encountering obstacles on the runout pad at the foot of the USGS debris flow flume. (a–d) Runup on a 5 m long, 30° adverse slope on 20 May 1997. (e–h) Runup on a 2.4 m high vertical wall on 21 June 1994. In each frame "*t*" denotes the time elapsed since the debris flow was released from the flume head gate about 90 m upslope (Table 1). The final frame in each sequence shows the time of maximum runup.

Froude numbers [cf. *Zanuttigh and Lamberti*, 2007]. The secondary waves exhibited consistent fractal number-size distributions, but the timing and amplitudes of individual waves were mostly random [*Iverson et al*., 2010]. Nevertheless, the largest secondary waves invariably trailed the flow fronts by several seconds. These large waves owed their origins partly to the effects of 0.3–0.6 m^3 of ponded water that collected behind the upper ends of the wet sediment prisms prior to their release from the flume head gate. Following gate release, the ponded water mixed with adjacent debris as it began to move downslope, enhancing its mobility. This water-rich debris overtook debris in front of it and thereby instigated development of a secondary wave that commonly grew to a height surpassing that of the leading wave at the flow front.

Table 1. Basic Geometric Attributes of Runup Experiments

Experiment Date	Debris Volume (m^3)	Obstacle Type	Vertical Obstacle Height (m)	Horizontal Obstacle Width (m)	*x* Coordinate of Base of Obstacle (m)	*x* Coordinate of Channel Sidewall Termination (m)
6-21-94	9.3[a]	vertical wall	2.4	5.2	91.0	87.4
6-23-94	10.1[a]	vertical wall	2.4	5.2	91.0	87.4
5-20-97	10.0[a]	30° slope	2.4	3.0	90.7[b]	91.0
5-22-97	9.9[a]	30° slope	2.4	3.0	90.7[b]	91.0

[a]Debris volumes indicate measured volumes of static sediment positioned behind the flume head gate at $x = 0$ m.
[b]The foot of the ramp forming the 30° adverse slope had an upward concave curvature, such that the slope varied smoothly from 0° at $x = 90.7$ m to 30° at $x = 91.5$ m.

The experimental debris flows decelerated and thickened as they exited the steep part of the flume. Deceleration occurred mostly between $x = 74$ m and $x = 84$ m, where the bed slope gradually diminished from 31° to 2.4°. Beyond $x = 84$ m, flow fronts as well as the largest secondary waves maintained speeds of roughly 10 m/s until they encountered the obstacles at $x \approx 91$ m (Table 1).

Sensor data and measurements on synchronized video recordings provide quantitative records of the time-dependent behavior of the incoming flows immediately prior to runup (Figures 6 and 7 and Data Sets S1–S4 in the supporting information). In the experiments with a 30° adverse slope (20 May 1997 and 22 May 1997), time series of flow velocities $u(t)$ were measured by tracking surface particles visible at $x = 89.5$ m, and time series of flow depths $h(t)$ were measured with an overhead laser ranging device positioned at $x = 90$ m. In order to calculate a corresponding time series of Froude numbers, $\mathrm{Fr}(t) = u(t)/\sqrt{gh(t)}$, we treated the data from these two positions as colocated and used measured surface velocities as surrogates for depth-

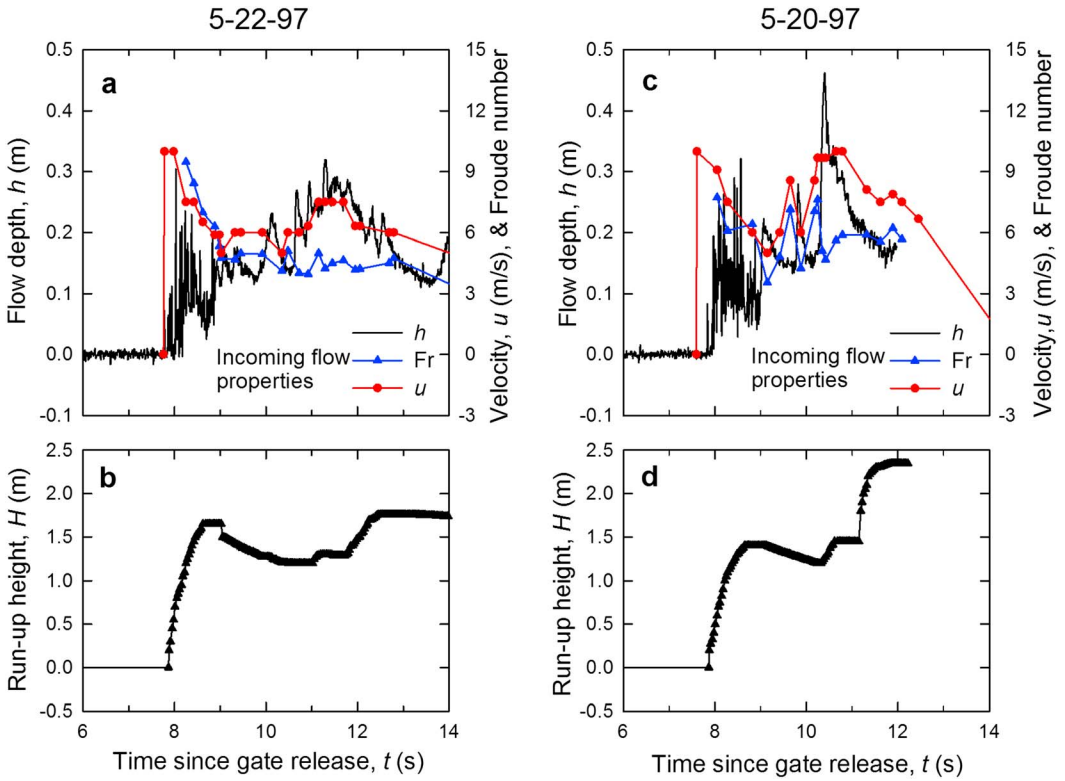

Figure 6. Measurements of time-dependent incoming flow properties and runup heights in two replicate experiments involving debris flow runup on a 30° adverse slope. In experiment 20 May 1997, unintentional shutdown of the digital data acquisition system occurred at $t = 11.98$ s, shortly after maximum runup occurred. Tabulated versions of the data graphed here are available in the supporting information as Data Set S3 and Data Set S4.

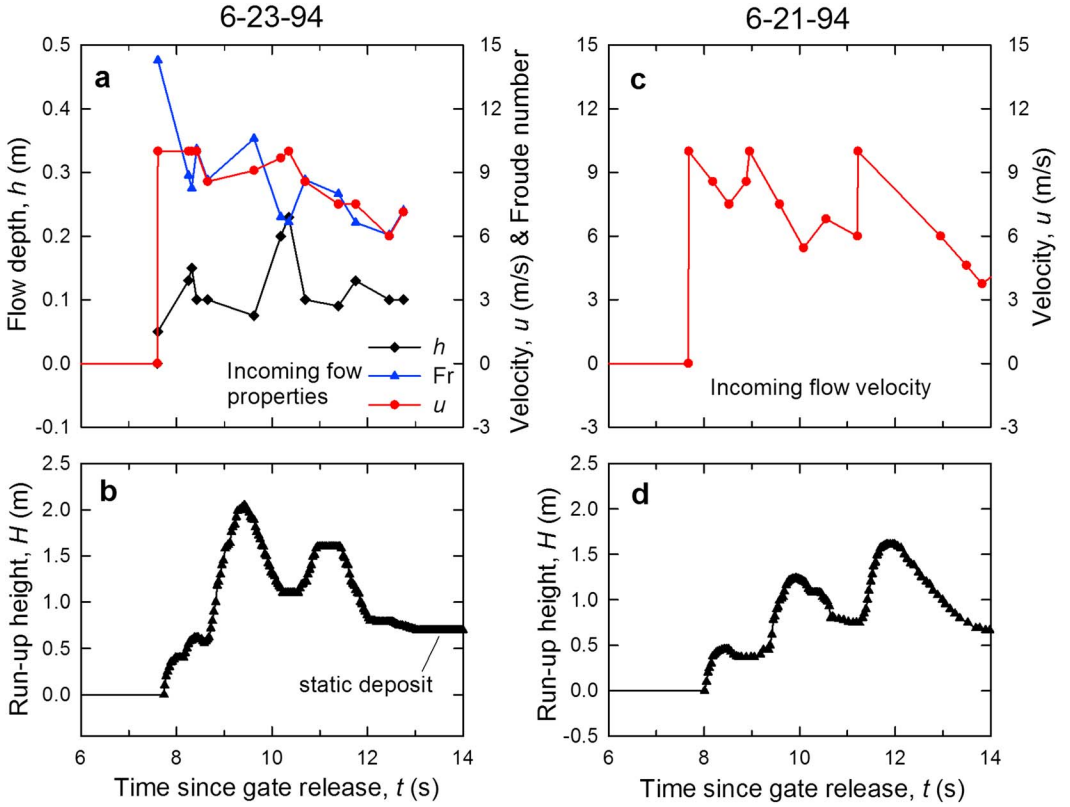

Figure 7. Measurements of time-dependent incoming flow properties and runup heights in two replicate experiments involving debris flow runup on a vertical barrier. No measurements of the incoming flow thickness *h* were possible for experiment 21 May 1994. Tabulated versions of the data graphed here are available in the supporting information as Data Set S1 and Data Set S2.

averaged velocities. The resulting values of Fr ranged from about 3 to 9 over the course of an experiment, and flow depths ranged from < 0.1 m to > 0.4 m (Figures 6a and 6c). In the experiments involving runup on a vertical barrier (21 June 1994 and 23 June 1994), all data were extracted from measurements on digitized video footage, and in one case (21 June 1994) the footage was inadequate to allow determination of flow depths and Froude numbers (Figure 7c). Despite these limitations, Figures 6 and 7 provide clear evidence that the typical speeds and depths of the incoming flows were consistent in each experiment—and that the passage of secondary waves caused fluctuations in speeds and depths that varied from case to case. In no case was incoming flow behavior at the measurement cross sections influenced by the presence of downstream obstacles until after maximum runup occurred.

3.2. Flow Behavior During Runup

Video recordings and stop-action photographs revealed qualitative features of runup behavior (Figure 5 and supporting information Movies S1–S4), and measurements on digitized video footage provided time series of runup heights (Figures 6b, 6d, 7b, and 7d). In each experiment, the first debris reached the obstacle just prior to $t = 8$ s. (Here and elsewhere in this paper, $t = 0$ denotes the time the flume head gate began to open.) The leading edge debris consisted of a dilute gravel spray at most a few centimeters thick that ran up a relatively short distance before collapsing downward. Within about 1 s the gravel spray was overridden by the first large wave of wet sand and gravel. This wave produced the first major peak in runup heights, which exceeded 1.2 m in each experiment (Figures 6b, 6d, 7b, and 7d). In the experiments with vertical barriers, runup of the leading wave appeared to be enhanced by the presence of the already-deposited gravel spray, which formed a small mound at the foot of the barrier and helped redirect some incoming flow momentum upward. Nevertheless, during runup, the leading large wave quickly broke backward as an upstream-propagating shock developed (e.g., Figure 5f).

In each experiment the arrival of the leading wave was followed 2–3 s later by arrival of the biggest secondary wave, which invariably produced peak runup heights >1.5 m (Figures 6b and 6d and and 7b and 7d). During runup on vertical barriers, the leading wave broke and mostly collapsed downward before this second big wave arrived. During runup on the 30° slope, the second big wave overtook and partially merged with the leading large wave while it was still on the slope. This merging of waves was accompanied by development of an upstream-migrating shock that appeared to suppress subsequent runup (e.g., Figure 5c). Another characteristic behavior was ejection of some isolated gravel clasts from the tip of debris flow waves during runup. These clasts seldom traveled more than 0.1 m higher than the continuous wave fronts, however, and they were omitted from consideration in determining runup heights.

In each experiment the maximum runup occurred at the flume centerline, but considerable debris was shunted laterally away from the centerline, indicating that mass and momentum fluxes were far from one dimensional (supporting information Movies S1–S4). Nevertheless, other features of runup behavior helped corroborate basic concepts embodied in the 1-D SMF and MJ models. For example, smooth upslope momentum transfer was sometimes conspicuous, and development of shocks was at other times conspicuous (Figure 5). Deviations from these idealized behaviors arose mostly from the effects of unsteady flow and wave interference.

From the standpoint of predicting runup, a key observation is that the time series of runup heights measured in pairs of replicate experiments were broadly similar to one another but differed in detail owing to variations in the timing and sizes of secondary waves. The experiments with a 30° adverse slope each produced a double-peaked sequence of runup heights, but in one case the two peaks were of nearly equal amplitude, while in the other case the second peak was about 1 m higher than the first peak (Figures 6b and 6d). Similarly, the experiments with a vertical barrier each produced a triple-peaked sequence of runup heights, wherein a minor initial peak produced by the flow front gravel spray was followed by two larger peaks, which had relative amplitudes that differed in the two experiments (Figures 7b and 7d). A clear implication of these variations in behavior is that accurate predictions of maximum runup heights require adequate information about of the sequence of incoming waves.

4. Tests of Analytical Predictions

To examine the merits of the analytical models quantitatively, it is useful to consider how well they predict the experimentally measured runup heights when the predictions are informed by a priori knowledge of the incoming flow properties. The need for detailed a priori knowledge limits the practical value of such predictions, but testing the predictions nevertheless provides physical insight. To perform such tests we use equations (1)–(4) to calculate values of H from the instantaneous values of u, h, and Fr shown in Figures 6a, 6c, and 7a. In graphing each of the resulting predictions shown in Figure 8, we add a 1 s time offset to account in a simple way for the elapsed time between the measurements of incoming flow properties and the time when the flow caused runup on obstacles a short distance downstream. The predictions of (3) and (4) shown in Figure 8 also utilize the values $\kappa = 1$ and $\phi_e = 40°$, because results obtained with these values suffice to illustrate trends that also arise with the use of other plausible values of κ and ϕ_e.

The most obvious inference from Figure 8 is that the MJ model commonly yields predictions that are better than those of the other models, whereas the FM model provides the poorest predictions. The superiority of the MJ model is particularly clear for predicting runup on the vertical barrier (Figure 8a), which caused abrupt flow stoppage and rapid shock development similar to that assumed in the model's derivation. On the other hand, for runup on the adverse slope (Figures 8b and 8c), it is difficult to ascertain whether the subtle differences in the misfits of the MJ and SMF models are the result of differences in mechanical assumptions or mere happenstance. The universally poor predictions of the frictionless FM model are noteworthy because they are even poorer than those of the frictionless PM model—despite the fact that the FM model is based on a more thorough accounting of energy conservation. Thus, we infer that both the PM and FM models are based on flawed assumptions. Consequently, the models have little intrinsic value for assessing runup behavior, and any correspondence between observed runup heights and predictions of these models is merely fortuitous.

Although Figure 8 provides evidence of the value of the MJ and SMF analytical models, the data portrayed in Figure 8 apply to flows that were neither steady nor one dimensional—violating a core assumption used to

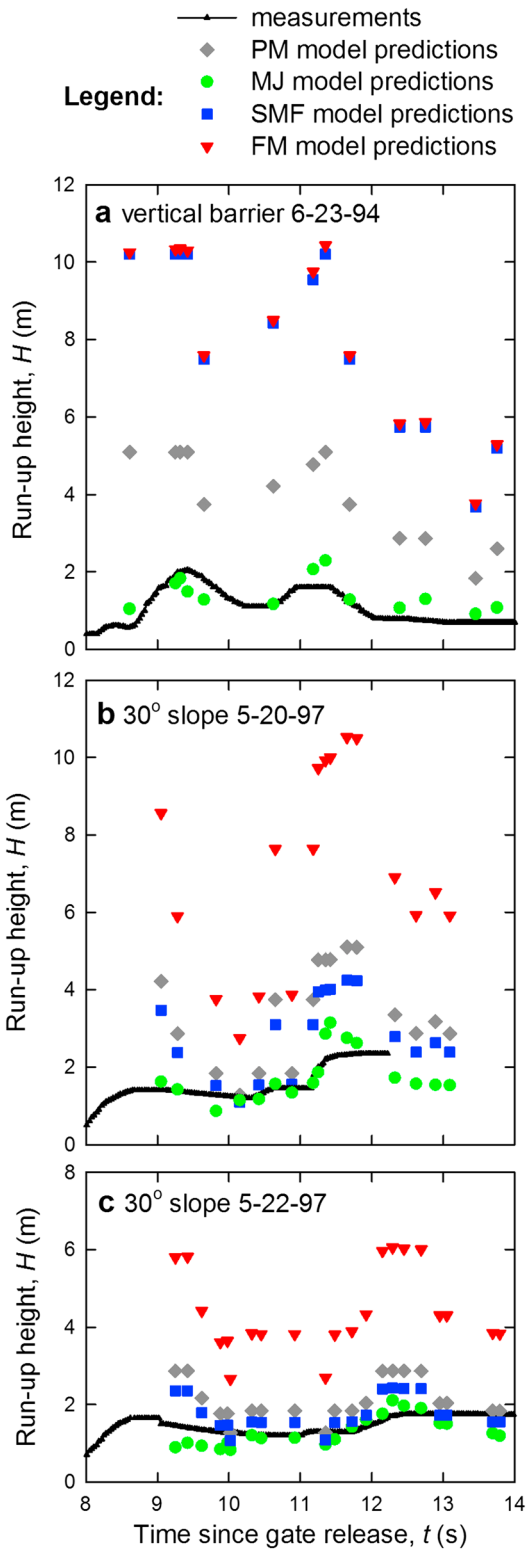

Figure 8. Comparison of evolving runup heights measured in experiments and runup heights predicted by four analytical models that utilize measurements of the evolving speeds and depths of incoming flows.

derive each of the models. Moreover, the model tests summarized in Figure 8 involved only two obstacle geometries. Therefore, a deeper examination of runup mechanics using a more sophisticated model is warranted.

5. Numerical Simulations and Model Tests

Our numerical simulations of runup differ fundamentally from our analytical predictions because they account for the dynamics of unsteady fluxes of mass and momentum within the flow body and flow front (Figure 9). As the spatially varying fluxes evolve, momentum jumps can develop naturally, but no assumptions about jump development are imposed. Moreover, unlike 1-D models, our 2-D numerical simulations account for lateral shunting of debris during runup.

We perform all of our numerical simulations by using D-Claw, a depth-integrated, shock-capturing model that blends concepts of soil mechanics, granular mechanics, and fluid mechanics to seamlessly simulate debris flow behavior from initiation to deposition. (The D-Claw code is available at https://github.com/dlgeorge/D-Claw-4.x.) *Iverson and George* [2014] provide a detailed derivation of the D-Claw equations, and *George and Iverson* [2014] describe our numerical method of solving the equations, as well as tests of model predictions against data from debris flow flume experiments that did not involve runup. Use of D-Claw to simulate the dynamics of a natural debris avalanche/flow that produced a modest distal runup is described by *Iverson and George* [2016].

In general D-Claw computes the coupled evolution of five dependent variables in space and time: the flow thickness, h, the depth-averaged velocity components parallel to the bed, u and v, the solid volume fraction, m, and the basal pore fluid

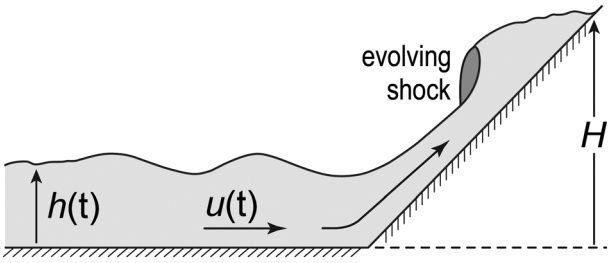

Figure 9. Schematic vertical cross section illustrating runup influenced by unsteady inflow conditions, as simulated by D-Claw.

pressure, p_b. For simple flow paths, such as those imposed by the geometry of the USGS debris flow flume and adjacent runout pad, the model equations are solved in a bed-fitted coordinate system. In this system h is the flow thickness normal to the bed, u is the downslope velocity component, and v is the cross-slope velocity component. The geometry of obstacles on the runout pad is represented by a function $z = b(x, y)$, where z denotes the elevation of the obstacle surface in a direction normal to the runout pad surface and x and y are downslope and cross-slope coordinates [*George and Iverson*, 2014]. The obstacle consequently forms a topographic feature superposed on an otherwise bed-normal coordinate system. Modeled flows engage basal Coulomb frictional that is locally reduced in proportion to any positive basal pore fluid pressure and locally increased by the presence of any upward terrain curvature, which generates a centrifugal force that increases the apparent weight and pressure within moving debris [*George and Iverson*, 2014].

Each of the 200 D-Claw simulations we summarize here uses the value $\kappa = 1$ for the longitudinal pressure coefficient. (Values of other model parameters in specific subsets of simulations are presented in sections 5.1, 5.2, and 6.) The value $\kappa = 1$ implies that internal pressures are isotropic—the simplest possible pressure distribution. Because we lack any data that demonstrate the superiority of alternative values of κ, the value $\kappa = 1$ provides a logical starting point when performing computational model tests. Moreover, $\kappa = 1$ yields good predictions of observed runup heights when the analytical MJ model is used in conjunction with empirical constraints on inflow properties (Figure 8). This finding provides further support for using the parsimonious assumption $\kappa = 1$ in a more sophisticated—and more complex—runup model such as D-Claw.

5.1. Tests of Runup Simulations That Use Known Inflow Kinematics

We first present numerical simulations that isolate predictions of runup from those of upstream flow dynamics. These simulations utilize a priori knowledge of the evolving thicknesses, $h(t)$, and velocities, $u(t)$, of the incoming experimental flows to compute predictions of the evolving runup height, $H(t)$. They consequently yield numerical predictions that are partly analogous to the analytical predictions summarized in Figure 8.

For simulations of runup on the 30° adverse slope, the time series data $h(t)$ and $u(t)$ shown in Figure 6 are imposed as inflow boundary conditions at $x = 89.5$ m, and for a simulation of runup on the vertical barrier, the time series data shown in Figure 7a are imposed at $x = 87.4$ m. The condition $v = 0$ is also imposed at these locations to reflect the initial confinement of flows between vertical sidewalls. These upstream boundary conditions can be imposed in a numerically stable fashion because the incoming flows are universally supercritical. During the simulations, flow disturbances caused by interactions with obstacles do not propagate upstream to the inflow boundaries.

No experimental data analogous to $h(t)$ and $u(t)$ exist to constrain the evolving values of the solid volume fraction $m(t)$ and basal pore fluid pressure $p_b(t)$ of the incoming flows. Therefore, we simplify this set of D-Claw simulations by stipulating that the solid volume fraction remains equal to its initial value (i.e., $m(t) = m_0 = 0.64$), and that the basal pore pressure is zero during the first 1.2 s of inflow and is subsequently hydrostatic (i.e., $p_b(t) = \rho_w g_z h(t)$). These specified inflow conditions mimic the effects of the relatively dry gravel spray observed at the fronts of the experimental flows as well as the pore pressure distributions typically observed in the wetter, thicker SG debris behind the gravel fronts [*Iverson et al.*, 2010]. The simulations also use experimentally measured values of the basal friction angle $\phi_{\text{bed}} = 28°$ and pore water viscosity $\mu = 0.001$ Pa s [*Iverson et al.*, 2010]. Other parameters typically used in D-Claw are irrelevant in these simulations because they omit the effects of coupled evolution of pore pressures and solid volume fractions.

The evolving runup heights computed in each simulation can be readily compared to experimental data by referencing the predictions to the opening time of the flume head gate (Figure 10). In both the experiments and model predictions, maximum runup occurs along the flow centerline. Regions of lower runup, which are

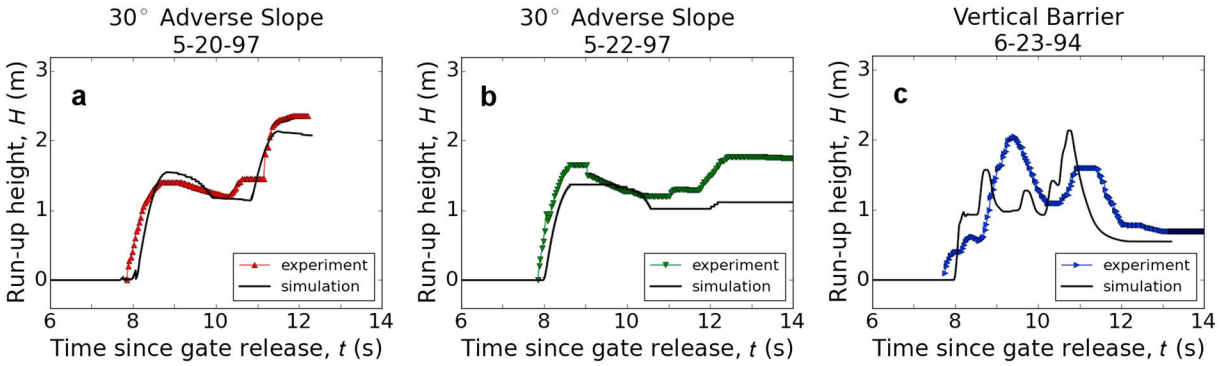

Figure 10. Comparison of measured and modeled evolution of runup heights for D-Claw numerical simulations in which unsteady incoming flow properties are specified a priori. *H* designates vertical runup height at the obstacle centerline.

symmetrically distributed about the centerline, are also observed in the experiments and predicted by the simulations (Figures 11 and 12 and Movies S5 and S6 in supporting information). Lateral shunting of debris into these regions broadens the areas affected by runup and reduces the peak runup heights relative to the heights computed in 1-D simulations that assume $v = 0$ applies and thereby neglect lateral shunting.

In general, the simulated runup behaviors illustrated in Figures 10–12 match the behaviors measured in the experiments quite well. Each simulated and measured time series has two major peaks (Figure 10). The first major peak is caused by the arrival of the leading wave of wet debris that trails the gravel-rich flow front, and the second is caused by the arrival of the largest secondary wave a few seconds later. For the vertical barrier experiment, the simulated and measured time series also exhibit a smaller preliminary peak associated with runup of the gravel spray at the leading edge of the flow (Figure 10c). The deposit formed by this gravel spray is additionally responsible for much of the model misfit evident in Figure 10c, because the gravel deposit was overridden by ensuing flow. The overriding was accompanied by upslope redirection of incoming flow momentum prior to the formation of a shock, thereby contradicting a premise and prediction of the depth-averaged D-Claw model (Figure 11).

Relative to the simulation of the vertical barrier experiment, D-Claw simulations of the adverse slope experiments yield better fits to the measured timing and amplitudes of major runup peaks (Figures 10a and 10b). Moreover, the D-Claw simulations largely reproduce the variations in behavior that distinguish the two adverse slope experiments. This result implies that the variations are explained well by variations in the inflow time series used to generate the simulations. Moreover, it implies that D-Claw provides a satisfactory representation of runup mechanics on adverse slopes if the incoming flow behavior is well-constrained.

5.2. Tests of Ab Initio Simulations of Flow Dynamics and Runup

We next present the results of ab initio numerical simulations of the runup experiments. The simulations test D-Claw's ability to predict runup if only the flume geometry and the initial configuration and properties of the static, water-saturated debris loaded behind the flume head gate are specified (Table 2). These conditions are held fixed in all simulations, which begin with the progressive opening of the head gate starting at $t = 0$ [cf. *George and Iverson*, 2014]. As the modeling debris flows descend the flume and run up on an obstacle, each of the dependent variables in D-Claw (u, v, h, p_b, and m) continuously evolves.

Independent measurements reported as part of the SG Smooth Bed data set of *Iverson et al.* [2010] constrain the values of all model parameters used in the simulations, with the exception of the lithostatic critical state solid volume fraction m_{crit} and longitudinal pressure coefficient κ (Table 2). For the sake of parsimony, each of the simulations uses the value $m_{crit} = 0.645$ to mimic the slightly loose initial state of the debris (with $m_{crit} - m_0 = 0.005$), and each uses the value $\kappa = 1$.

Because the ab initio simulations predict the behavior of incoming flows in addition to predicting runup, they afford opportunities for an expanded suite of model tests. Comparisons of predicted and measured flow thickness time series can be made for three locations upslope of the runup obstacles (Figure 13). For two locations within the steeply sloping part of the flume, at $x = 32$ m and $x = 66$ m, comparisons can be made by

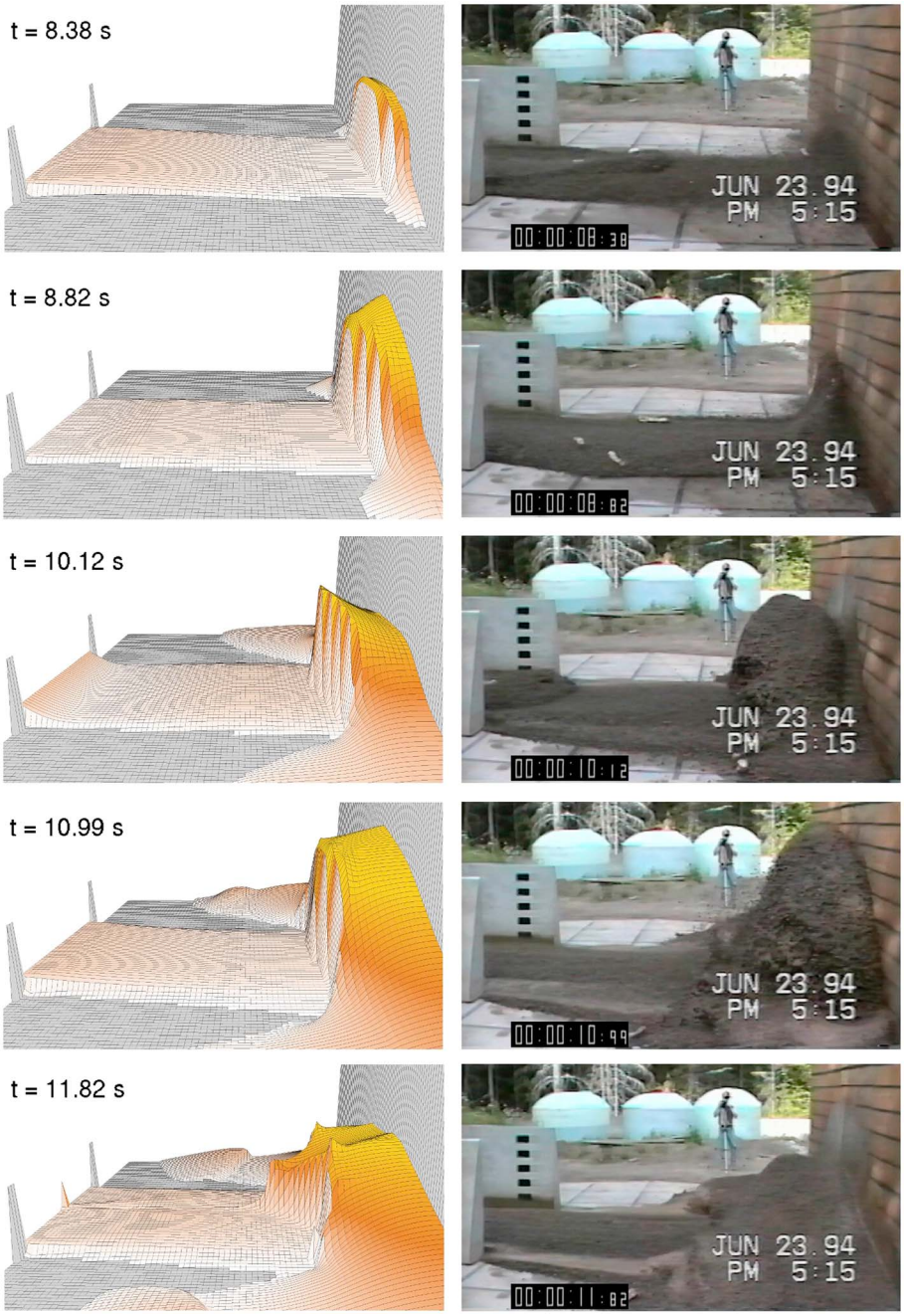

Figure 11. (left column) Oblique 3-D perspective views of D-Claw simulations and (right column) corresponding video frame captures of vertical barrier runup experiment 23 June 1994. Measured incoming flow properties are used to initiate the simulation. Timestamp in each frame of model results and video recordings refers to the time since the flume head gate began to open. An animated version of this figure is available as Movie S5 in supporting information.

using the aggregated data set for the 11 SG smooth bed experiments of *Iverson et al*. [2010]. For the cross section at $x = 89.5$ m, near the foot of the adverse slope, comparisons can be made by using the data shown in Figure 6. (Analogous data collected in the vertical barrier experiments are not useful for this purpose owing to their limited resolution, which is illustrated in Figure 7.) The simulations successfully predict the main features of the evolving speeds and thicknesses of the debris flows measured at $x = 32$ m and $x = 66$ m (Figures 13a and 13b). However, they do not predict the development of secondary waves that produce thickness fluctuations in regions behind the flow front.

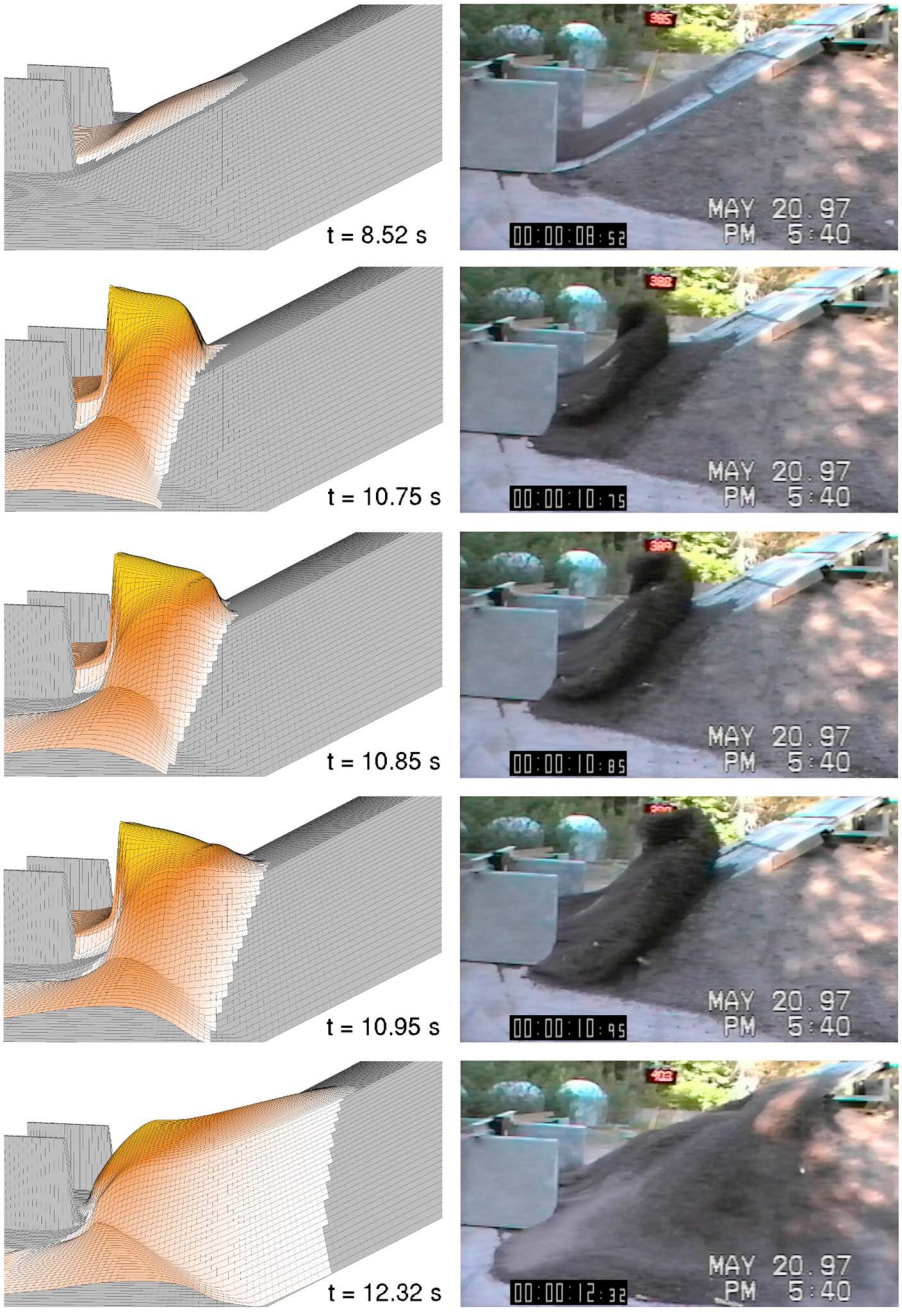

Figure 12. (left column) Oblique 3-D perspective views of D-Claw simulations and (right column)corresponding video frame captures of adverse slope runup experiment 20 May 1997. Measured incoming flow properties are used to initiate the simulation. Timestamp in each frame of model results and video recordings refers to the time since the flume head gate began to open. An animated version of this figure is available as Movie S6 in Supporting Information.

The model results and data show that the effects of flow thickness fluctuations are amplified when the debris flows closely approach the foot of the adverse slope. The simulated speed and thickness of the flow front at $x = 89.5$ m compare well with measurements, but the simulated behavior behind the flow front differs from measured behavior in two prominent ways (Figure 13c). First, the simulations do not reproduce the thickness fluctuations that accompany the arrival of secondary waves from about $t = 9$ to 12 s. Second, the simulations predict that debris that has previously run up the slope recedes downslope and produces an upstream-propagating shock that abruptly increases the flow thickness nearly sixfold when the shock reaches

Table 2. Comparison of Parameter Values in the SG Smooth Bed Experiments of *Iverson et al.* [2010] and Values Used in Ab Initio D-Claw Simulations Reported Here

Property	Measured Values	Model Values
Initial solid volume fraction, m_0	0.64	0.64
Lithostatic critical state solid volume fraction, m_{crit}	none	0.645
Basal friction angle of debris, ϕ_{bed} (°)	28	28
Initial debris hydraulic permeability, k_0 (m^2)	$1 \times 10^{-11} - 5 \times 10^{-10}$	1×10^{-11}
Debris compressibility index, a[a]	0.05	0.05
Pore fluid viscosity (water), μ (Pa s)	0.001	0.001
Pore fluid density (water), ρ_f (kg/m^3)	1000	1000
Solid grain density, ρ_s (kg/m^3)	≈ 2700	2700
Longitudinal pressure coefficient, κ	none	1

[a]In D-Claw a is related to the evolving mixture compressibility α by the equation $a = \alpha[m(\sigma_e + \sigma_0)]$, where m is the ambient solid volume fraction, σ_e is the ambient basal effective normal stress, and σ_0 is a baseline normal stress with the fixed value $\sigma_0 = 1000$ Pa.

$x = 89.5$ m at $t \approx 12$ s. A smaller upstream-propagating shock that reaches $x = 89.5$ m at $t \approx 14$ s is evident in the data and is visible in video footage for the 22 May 97 experiment (supporting information Movie S4). Differences in the predicted and observed shock timing and amplitude arise from the simulation's lack of secondary waves.

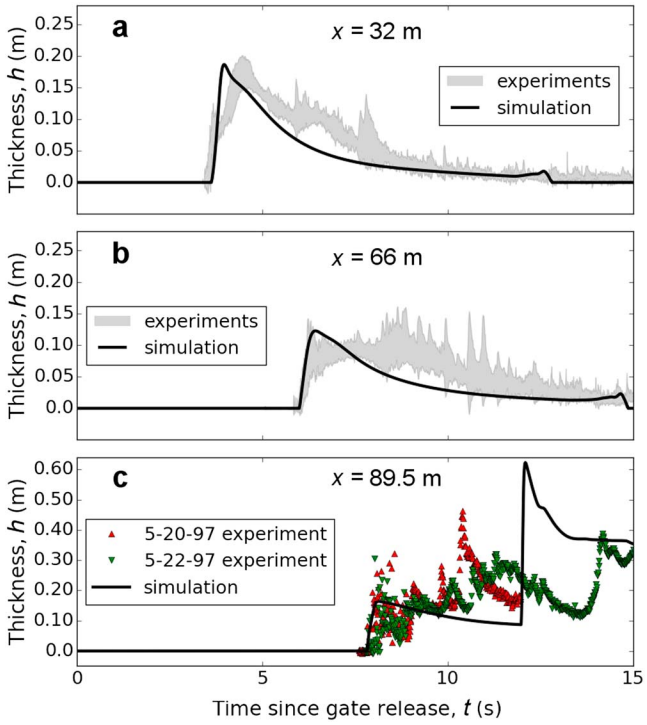

Figure 13. Comparison of evolving flow thicknesses predicted by ab initio numerical simulations with those measured at three locations upstream of the adverse slope at $x = 90.7$ m (where x denotes the downslope distance from the flume head gate). (a and b) The gray bands depict the measured mean flow thickness ±1 standard deviation for an aggregated data set compiled for the 11 SG Smooth Bed experiments of *Iverson et al.* [2010]. Tabulated versions of those data are linked to that publication.

Comparisons of predicted and measured runup heights show that the ab initio predictions of the time when runup begins are nearly exact (Figure 14). However, the simulations predict the existence of a single large pulse of runup, whereas the data from each experiment have a double-crested peak due to the presence of secondary waves. The lack of secondary waves and gravel-rich flow fronts in the simulations generates maximum runup height predictions that are too large in the case of the adverse slope experiments and too small in the case of the vertical barrier experiment. The maximum prediction error is about 70%. This shortcoming of the ab initio simulations is linked to their lack of grain size segregation effects, which are responsible for the development and growth of gravel-rich flow fronts as well as secondary waves.

Despite their shortcomings, the ab initio simulations nevertheless produce runup behavior that appears realistic because it includes the effects of evolving, 2-D momentum fluxes and lateral shunting of debris (Figures 15 and 16 and supporting information Movies S7 and S8).

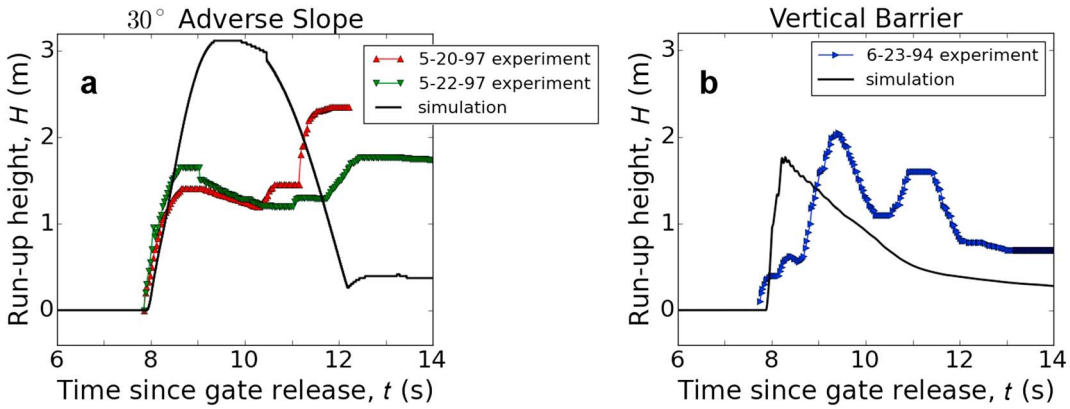

Figure 14. Comparison of evolving runup heights predicted by ab initio numerical simulations with those measured in two adverse slope experiments and one vertical barrier experiment.

Predicted runup heights are sufficiently accurate that the underlying physics are clarified rather than obscured. Furthermore, the simulations account for coupled evolution of the solid volume fraction, basal pore pressure, and effective friction during runup. No data currently exist to test these aspects of model predictions, but the predicted behavior of multiple, coevolving variables expands the prospects for future model tests.

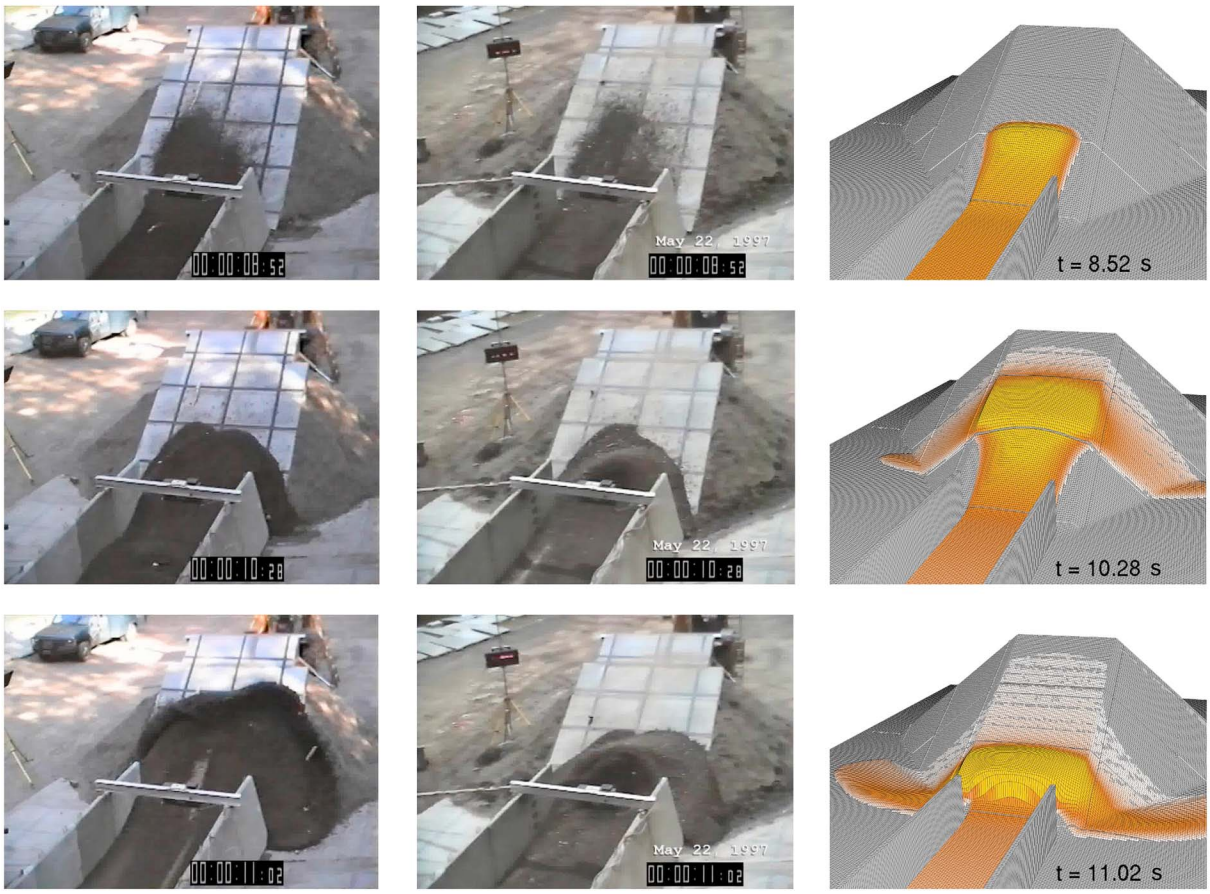

Figure 15. (right column) Oblique 3-D perspective views of ab initio D-Claw simulation and (left columns) corresponding video frame captures for two adverse slope runup experiments. Timestamp in each frame of model results and video recordings refers to the time since the flume head gate began to open. An animated version of this figure is available as Movie S7 in supporting information.

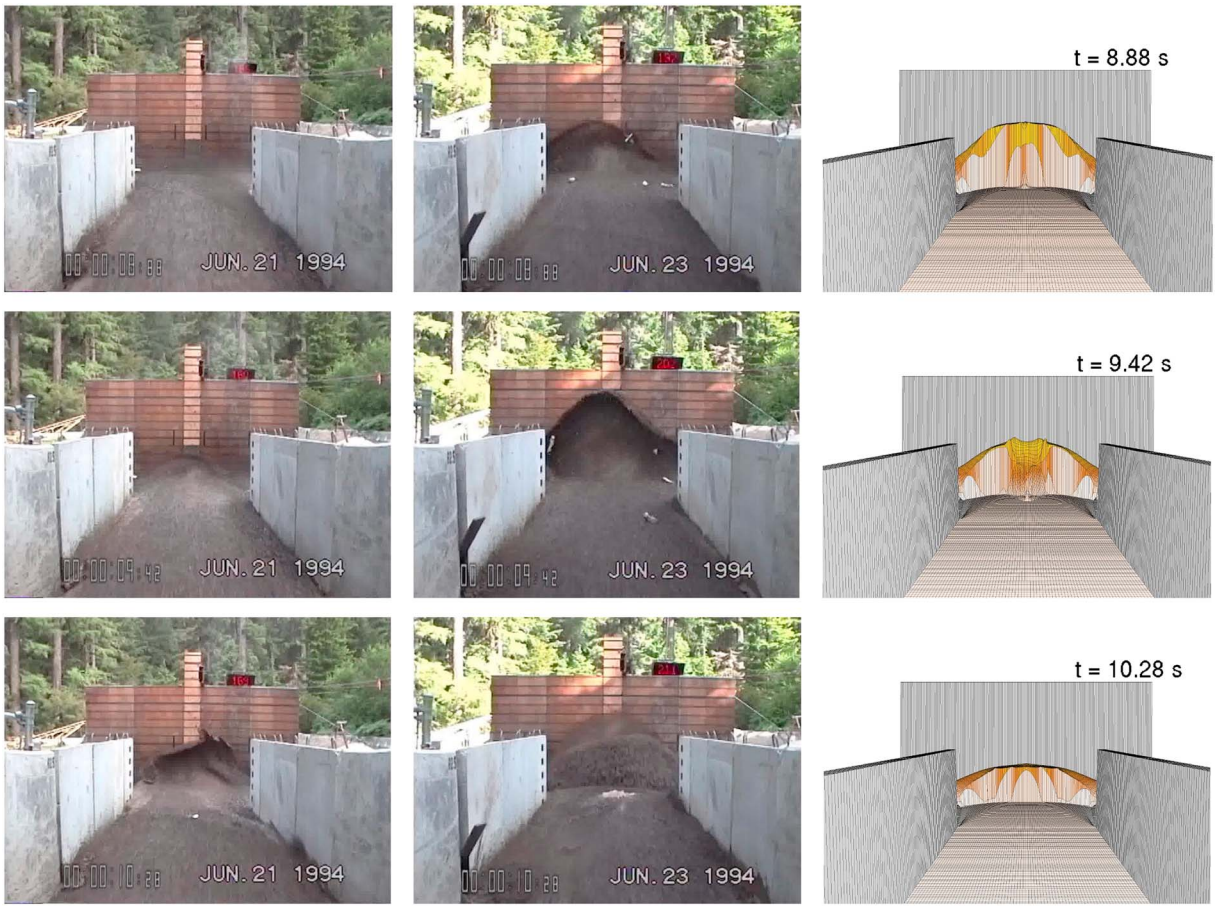

Figure 16. (right column) Oblique 3-D perspective views of ab initio D-Claw simulation and (left columns) corresponding video frame captures for two vertical barrier runup experiments. Timestamp in each frame of model results and video recordings refers to the time since the flume head gate began to open. An animated version of this figure is available as Movie S8 in supporting information.

6. Comparison of Runup Prediction Methods

Runup mechanics are distilled most clearly in 1-D analytical models, but runup predictions that are more detailed and versatile—and generally more accurate— result from numerical modeling of unsteady, multi-dimensional flows. Here to gain a deeper understanding of relationships between runup mechanics and runup predictions, we consider scenarios in which predictions of the SMF, MJ, FM, and PM analytical models can be compared directly with numerical predictions of D-Claw. For each scenario we use D-Claw to compute the maximum runup produced by a steady, uniform, homogenous, 1-D flow, and we compare the resulting predictions with those of analytical models that use the same inflow assumptions and parameter values (Figure 17).

The upstream boundary condition used in these idealized D-Claw simulations stipulates that a steady, frictionless, incoming flow impinges continuously on the foot of an obstacle, which exerts frictional resistance governed by an effective basal friction angle ϕ_e. The simulations each assume that $m = m_0$, $p_b = 0$, and $\kappa = 1$, implying that ϕ_e completely determines basal flow resistance during runup. The value $u_0 h_0 = 1$ m^2/s is held fixed in each simulation, while the value of Fr_0 is manipulated to account for combined variations in the inflow velocity u_0 and thickness h_0. Because these 1-D simulations prohibit flow in the cross-stream direction, only the downstream flow velocity, $u(x, t)$, and the bed-normal flow thickness, $h(x, t)$, evolve during runup. The simulations continue until $t = t_{\mathrm{stop}}$, when the maximum normalized runup height $H/(u_0^2/g)$ is attained. Predicted values of $H/(u_0^2/g)$ are independent of the debris flow scale, whereas predicted values of t_{stop} are specific to the scale implied by $u_0 h_0 = 1$ m^2/s. This value of $u_0 h_0$ provides a suitable proxy for

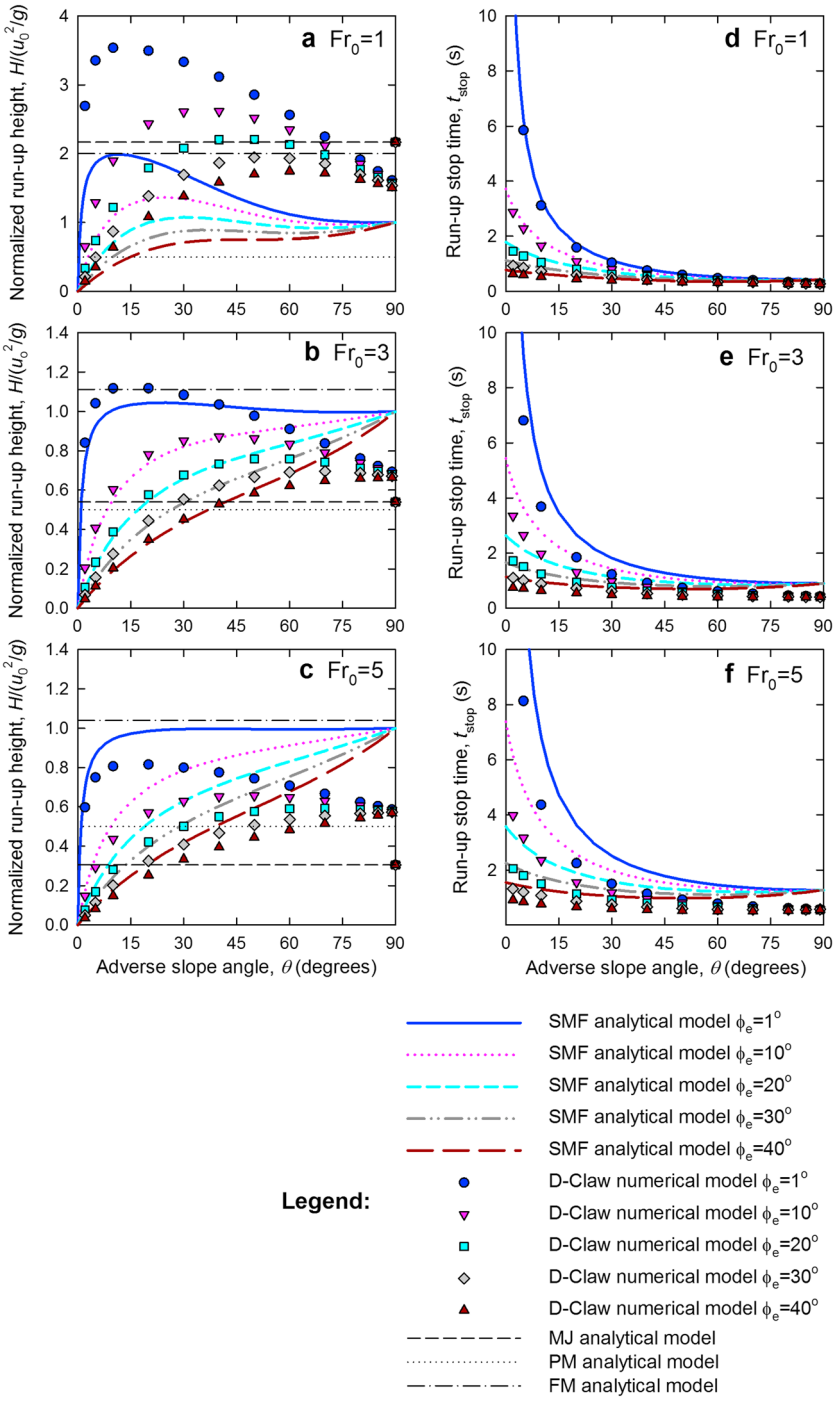

Figure 17. Comparison of normalized runup heights and runup stop times predicted by the D-Claw numerical model and four analytical models: the smooth momentum flux (SMF) model, the momentum jump (MJ) model, the point mass (PM) model, and the finite mass (FM) model. All predictions assume steady, uniform, one-dimensional inflow.

typical inflow conditions in our debris flow flume experiments, but larger values would generally be suitable for large-scale geophysical phenomena (e.g., Figure 1).

Figure 17 summarizes the analytical predictions of equations (1)–(4) which are shown by smooth curves and straight lines, as well as the predictions of 195 D-Claw simulations, which are shown by discrete points. Panels on the left side of Figure 17 illustrate predicted normalized runup heights for widely ranging values

of Fr_0, θ, and ϕ_e, and Figures 17d–17f illustrate corresponding predictions of t_{stop}. (Among the four analytical models, only the SMF model predicts t_{stop} and thereby affords an opportunity for comparison with numerical results (Appendix B).) For purposes of comparison, we treat the D-Claw predictions as accurate and treat the analytical predictions as estimates based on their more severe approximations of the pertinent physics.

The SMF model yields predictions of $H/(u_0^2/g)$ and t_{stop} that broadly resemble those of D-Claw; the two models predict similar nonlinear dependencies of runup behavior on the adverse slope angle θ and effective basal friction angle ϕ_e (Figure 17). However, the SMF model yields $H/(u_0^2/g)$ values that are generally too small if $Fr_0 = 1$ and too large if $Fr_0 = 5$, while they are more accurate if $Fr_0 = 3$. The differences in the SMF and D-Claw predictions of $H/(u_0^2/g)$ can be explained partly on the basis of subtle but systematic differences in their predictions of t_{stop} (Figure 17). However, the differences also result from the effects of longitudinal momentum advection within the head of the flow during runup. This advection is represented in the D-Claw simulations but not in the SMF model, which accounts for momentum transfer from the flow body to the flow head but not for momentum redistribution within the head itself. For cases with $Fr_0 = 1$, in which both models yield comparable predictions of t_{stop} (Figure 17d), the D-Claw predictions of $H/(u_0^2/g)$ are roughly twice as large as those of the SMF model owing to the effects of momentum advection that helps propel the tip of the flow head upslope. As the value of Fr_0 increases, however, the duration of momentum advection simulated in D-Claw is shortened by increasingly rapid formation of a shock that limits the runup height. Consequently, for $Fr_0 = 5$ as well as for larger values of Fr_0, the SMF predictions of $H/(u_0^2/g)$ are larger than those of D-Claw. These trends indicate that the essential physics of runup involve the competing effects of upslope momentum fluxes, which boost runup, and shock formation, which limits the process.

In contrast to the SMF and D-Claw predictions, the predictions of the MJ, FM, and PM models have no dependence on the values of θ and ϕ_e (Figure 17). However, as $\theta \rightarrow 90°$, the D-Claw predictions of $H/(u_0^2/g)$ converge toward values that are approximated better by the MJ model than by the SMF model. Indeed, for $\theta = 90°$, D-Claw predictions of $H/(u_0^2/g)$ precisely match those of the MJ model. This result is unsurprising, because a simulated flow that impinges against a vertical barrier immediately loses all of its downstream momentum and develops a shock in response. The overall trends in the D-Claw predictions indicate that shock development plays an increasingly prominent role as the adverse slope angle steepens.

Finally, it is noteworthy that the maximum runup heights predicted by each of the five models have considerable overlap, particularly for cases with $\theta \leq 45°$ (Figure 17). Consequently, the maximum runup heights observed on moderate adverse slopes may not suffice to distinguish between the predictive values of alternative models. This finding indicates that some of the relatively good predictions of the MJ and SMF models shown in Figure 8b and 8c might be due more to happenstance than to applicability of their simplified physics.

7. Discussion

The work we report here focuses on the dynamics and prediction of runup caused by supercritical debris flows that encounter obstacles broad enough and high enough to stop downstream flow and cause a lateral redirection of momentum. Such obstacles may comprise either manmade barriers or natural terrain features similar to that shown in Figure 1. If incoming flows are subcritical, then the maximum runup heights they produce may depend on the progressive accumulation of mass behind obstacles rather than on the dynamics we investigate here. Furthermore, if obstacles are sufficiently narrow that flows can bypass them laterally, then the runup dynamics may differ from those we report.

Relative to the simplified 1-D analytical models we consider, D-Claw provides superior predictions of debris flow runup behavior. Its superiority derives from the fact that D-Claw accounts for continuously evolving distributions of mass and momentum, for lateral shunting of decelerating debris, and for the natural emergence of shocks during runup. D-Claw predictions are particularly accurate if they are informed by a priori knowledge of the dynamics of incoming flows. This accuracy is perhaps surprising because, like all depth-averaged models, D-Claw neglects the effects of vertical (or bed-normal) accelerations. These accelerations doubtlessly influence the runup process, but our results imply that neglect of the accelerations may not pose a serious shortcoming.

Use of depth-averaged models for runup forecasting is attractive because computations with such models can be orders of magnitude faster than computations with full 3-D models. None of the D-Claw simulations we report here required more than 10 min of CPU time on an ordinary desktop computer. Computation speed is particularly important if a probabilistic approach is used to compute a spectrum of possible runup scenarios that reflect uncertainties in initial data. Indeed, the variability of the runup behavior exhibited in our replicate experiments with nominally identical initial conditions implies that practical runup forecasting should include a probabilistic component.

The greatest limitation of D-Claw as a tool for ab initio runup prediction arises from its lack of representation of grain size segregation processes and effects. Size segregation produces debris flows' characteristic heterogeneous architecture, typified by coarse-grained, high-friction flow heads that are followed by finer grained, partially liquefied flow bodies [*Iverson*, 1997; *Johnson et al*., 2012]. Even more importantly, perhaps, size segregation strongly influences the development and behavior of secondary waves in debris flows [*Zanuttigh and Lamberti*, 2007; *Iverson et al*., 2010], and our experimental data demonstrate the crucial effect these waves can have on runup. The effect might be more or less pronounced in natural debris flows that include boulders with diameters comparable to the flow depth. Therefore, improvements in runup prediction using depth-averaged debris flow models will likely be contingent on development of a satisfactory means to incorporate the effects of grain size segregation.

8. Conclusions

The findings we report in this paper support the following conclusions:

1. Runup of supercritical debris flows on vertical barriers and adverse slopes involves time-dependent dynamics that are sensitive to the behavior of secondary waves as well as the leading wave in incoming flows. Variability in secondary waves and consequent runup behavior occurs even in replicate large-scale experiments with very similar initial conditions, flow front speeds, and peak flow depths.
2. Runup behavior is influenced by both smooth upslope momentum fluxes and abrupt momentum jumps. As the adverse slope angle and flow Froude number increase, jump development plays an increasingly important role in determining the maximum runup height. For moderate adverse slopes, where the effects of upslope momentum fluxes and basal friction supersede those of momentum jumps, longitudinal advection of momentum within the decelerating flow head conveys momentum to the tip of the head and enhances the maximum runup height.
3. As the Froude number of an incoming flow increases, the maximum runup height H increases monotonically, but the runup efficiency gauged by $H/({u_0}^2/g)$ decreases. These trends are consistent irrespective of whether runup behavior is dominated by a smooth upslope momentum flux or an abrupt momentum jump.
4. The effects of smooth upslope momentum fluxes and abrupt momentum jumps during runup are distilled most clearly in simple, steady state, 1-D analytical models that isolate their influences. In some circumstances the simple analytical models can provide reasonably accurate runup predictions—provided that the predictions are informed by a priori knowledge of the unsteady dynamics of incoming flows. In other circumstances predictions of these models are inherently poor owing to their neglect of the interplay between momentum fluxes and momentum jumps as well as their neglect of lateral shunting of debris during runup.
5. Superior predictions of runup heights and dynamics are provided by 2-D, depth-averaged numerical simulations that allow but do not enforce the development of momentum jumps and lateral shunting of debris. Like analytical predictions, numerical runup predictions using our D-Claw model are most accurate if they are informed by a priori knowledge of the unsteady dynamics of incoming flows, including the distribution of basal pore fluid pressure (and hence of basal friction). The lack of bed-normal acceleration effects in the depth-averaged simulations does not appear to be a major liability for runup prediction. Similarly, the assumption of isotropic pressures (i.e., $\kappa = 1$) used in each of our D-Claw simulations does not appear to be a liability.
6. Ab initio D-Claw simulations, which compute runup based on knowledge of only the flow path and obstacle geometries and the initial properties of static source debris, have predictive accuracy that is limited mostly by the simulations' inability to predict the features of secondary waves. This limitation is

associated with the model's lack of grain size segregation effects, because development and growth of secondary waves in debris flows is typically associated with grain size segregation.

7. Owing to the sensitive dependence of runup behavior on initial conditions and to the difficulty of predicting sequences of secondary waves, practical runup prediction warrants a probabilistic modeling strategy. Such a strategy is most readily implemented if computations are fast enough to enable large numbers of alternative simulations to be performed rapidly. Rapid computation is a virtue of depth-averaged numerical models.
8. Lastly, it is notable that the commonly used point mass (PM) runup formula, $H = u_0^2/2g$, universally provides a poor representation of runup dynamics, and it typically yields poor predictions of runup heights. It provides similarly poor estimates of inflow velocities based on observed runup heights. The momentum jump (MJ) and smooth momentum flux (SMF) models provide alternatives that are superior to the PM model if simple analytical approaches are used to estimate inflow velocities based on runup heights.

Appendix A: Derivation of Momentum Jump (MJ) Runup Formula

Standard jump conditions expressing conservation of mass and linear momentum across a shock that develops in a one-dimensional flow with depth-invariant velocity u, surface elevation h, and bulk density ρ may be expressed as [cf. *Jóhannesson et al.*, 2009, p. 81]

$$[\rho_0 h_0 (u_0 - s)] - [\rho_1 h_1 (u_1 - s)] = 0, \tag{A1}$$

$$\left\{[\rho_0 h_0 u_0 (u_0 - s)] - \int_b^{b+h} \sigma_0 \mathrm{d}z\right\} - \left\{[\rho_1 h_1 u_1 (u_1 - s)] - \int_b^{b+h} \sigma_1 \mathrm{d}z\right\} = 0, \tag{A2}$$

where subscript 0 denotes properties of the flow upstream of the shock, subscript 1 denotes properties of the flow downstream from the shock, σ denotes the longitudinal normal stress (defined as positive in tension), b denotes the bed elevation, and s denotes the shock speed. In applications involving flow runup against obstacles that cause static material to accumulate between the obstacle and the shock, these equations simplify because $u_1 = 0$. In this case the mass jump condition (A1) reduces to

$$s = \frac{-u_0}{(\rho_1 h_1/\rho_0 h_0) - 1}, \tag{A3}$$

which indicates that the shock travels upstream (opposite to the direction of u_0) if $\rho_1 h_1 \geq \rho_0 h_0$ (Figure 2b). Furthermore, use of (A3) along with the condition $u_1 = 0$ reduces the momentum jump condition (A2) to

$$\rho_0 h_0 u_0 \left(u_0 + \frac{\rho_0 h_0 u_0}{\rho_1 h_1 - \rho_0 h_0}\right) - \int_b^{b+h} \sigma_0 \mathrm{d}z + \int_b^{b+h} \sigma_1 \mathrm{d}z = 0. \tag{A4}$$

The next step in simplification involves approximation of the longitudinal normal stresses by

$$\sigma = -\kappa \rho g (z - b), \tag{A5}$$

where κ is a longitudinal pressure coefficient that equals 1 if normal stresses are isotropic but might plausibly range from about 0.2 to 5 [*Iverson and Denlinger*, 2001]. Both κ and ρ are assumed to be independent of z. Substitution of (A5) in (A4) and evaluation of the integrals then reduces (A4) to

$$\rho_0 h_0 u_0 \left(u_0 + \frac{\rho_0 h_0 u_0}{\rho_1 h_1 - \rho_0 h_0}\right) + \frac{1}{2}\kappa \rho_0 {h_0}^2 - \frac{1}{2}\kappa \rho_1 {h_1}^2 = 0. \tag{A6}$$

Algebraic reduction of (A6) involves several steps, which begin with multiplication of all terms by $\rho_1 h_1 - \rho_0 h_0$, proceed with cancellation of redundant terms and division of all remaining terms by $\rho_1 g h_0 h_1$, and conclude with multiplying these terms by h_1/h_0. These manipulations yield a cubic equation for h_1/h_0:

$$\frac{\rho_1}{\rho_0}\left(\frac{h_1}{h_0}\right)^3 - \left(\frac{h_1}{h_0}\right)^2 - \left(\frac{2}{\kappa}\,\mathrm{Fr}_0^{\,2} + 1\right)\left(\frac{h_1}{h_0}\right) + \frac{\rho_0}{\rho_1} = 0, \tag{A7}$$

where $\mathrm{Fr}_0 = u_0/\sqrt{g h_0}$. For the special case with $\kappa = 1$, (A7) is equivalent to equation (4) of *Hákonardóttir et al.* [2003] and to equation (11.15) of *Jóhannesson et al.* [2009]. For physically relevant parameter values ($\rho_1/\rho_0 \sim 1$, $0.2 \leq \kappa \leq 5$, $\mathrm{Fr}_0 \geq 1$), (A7) has three real roots, but only one of these roots has physical relevance by virtue of being positive and satisfying the jump-condition requirement that $h_1 > h_0$.

The relationship of (A7) to alternative runup formulas can be clarified by setting $\rho_1 = \rho_0$ and identifying h_1 as the runup height H. With these substitutions (A7) can be manipulated algebraically to obtain the runup formula (3) listed in the main text. This formula is implicit, however, because it contains H on the right-hand side. Thus, constructing graphs of (3) requires finding the roots of the cubic equation (A7). For this purpose we used *WolframAlpha* software that is freely available online.

Appendix B: Derivation of Smooth Momentum Flux (SMF) Runup Formula

Our analysis builds on an analysis presented by *Takahashi and Yoshida* [1979] and subsequently elaborated by *Hungr and McClung* [1987], *Chu et al.* [1995], and *Mancarella and Hungr* [2010], but it modifies the approach of these earlier analyses in three key respects. First, it assumes that all incoming flow momentum is redirected upslope by centripetal forces that act at the foot of the adverse slope. (Earlier analyses assumed that the vector component of incoming flow momentum that was not directed upslope vanished at the foot of the slope.) Second, it focuses on basal flow resistance caused exclusively by Coulomb friction, and third, it provides a more precise treatment of the effects of longitudinal pressure gradients than has been provided in the past.

Consider a flow head that has a time-dependent length $L(t)$, bed-normal thickness $h(x,t)$, and spatially uniform bulk density $\rho(t)$ as it runs up an adverse slope (Figure 2c). Thus, the evolving mass of the head is $\rho\overline{h}L$ per unit width, where $\overline{h} = (1/L)\int_0^L h\mathrm{d}x$ is the spatially averaged value of h. Mass balance requires that the total rate of change of $\rho\overline{h}L$ equals the incoming steady mass flux $\rho_0 h_0 u_0$ (per unit width) at the base of the slope, such that

$$\frac{\mathrm{d}\left(\rho\overline{h}L\right)}{\mathrm{d}t} = \rho_0 h_0 u_0 \tag{B1}$$

applies. This mass balance equation has a simple solution,

$$\rho\overline{h}L = \rho_0 h_0 u_0 t, \tag{B2}$$

which satisfies the relevant initial condition, $\rho\overline{h}L(0) = 0$.

As the head's mass evolves, its upslope velocity and linear momentum parallel to the bed also evolve. Evolution of the head's total linear momentum per unit width $\rho\overline{h}L\overline{u}$ obeys Newton's second law,

$$\frac{\mathrm{d}\left(\rho\overline{h}L\overline{u}\right)}{\mathrm{d}t} = F, \tag{B3}$$

where $\overline{u}$ is the mean upslope velocity within the head and F is the sum of all slope-parallel forces per unit width acting on the head. A detailed expression for F is

$$F = \rho_0 h_0 {u_0}^2 + \int_{x=0}^{L}\left[-\rho g h\sin\theta - \rho g h\cos\theta\tan\phi_e - \kappa\,\rho g h\cos\theta\frac{\partial h}{\partial x}\right]\mathrm{d}x, \tag{B4}$$

where $\rho_0 h_0 {u_0}^2$ is the incoming momentum flux per unit width due to debris arriving from upstream, $-\rho g h\sin\theta$ is the downslope component of the gravitational body force per unit area, $-\rho g h L\cos\theta\tan\phi_e$ is the downslope basal friction force per unit area, and $-\kappa\rho g h\cos\theta(\partial h/\partial x)$ is the longitudinal pressure force per unit area due to longitudinal variations in h [cf. *Savage and Hutter*, 1989]. Evaluation of the integral in (B4) yields

$$F = \rho_0 h_0 {u_0}^2 - \rho g\overline{h}L\sin\theta - \rho g\overline{h}L\cos\theta\tan\phi_e + \frac{1}{2}\kappa\rho g {h_0}^2\cos^3\theta, \tag{B5}$$

in which the final term incorporates the result

$$\int_0^L h\frac{\partial h}{\partial x}dx = \left[\frac{h^2}{2}\right]_0^L = -\frac{1}{2}(h_0\cos\theta)^2, \tag{B6}$$

where $h = h_0\cos\theta$ is the thickness of the flow head at $x = 0$ (i.e., at the foot of the adverse slope) and $h = 0$ is the thickness of the flow head at $x = L$.

Substitution of (B2) and (B5) into (B3), followed by some algebraic rearrangement, reduces the momentum balance for the flow head to

$$\frac{\mathrm{d}(\overline{u}t)}{\mathrm{d}t} = t\frac{\mathrm{d}\overline{u}}{\mathrm{d}t} + \overline{u} = -Gt + J, \tag{B7}$$

where

$$G = g(\sin\theta + \cos\theta\tan\phi_e) \tag{B8}$$

and

$$J = u_0 + (\kappa/2)(\rho/\rho_0)(gh_0/u_0)\cos^3\theta \tag{B9}$$

are constant coefficients. The solution of (B7) is $\overline{u} = (1/t)[-(1/2)Gt^2 + Jt + c]$, where c is a constant of integration. The solution has a regular singular point at $t = 0$, but the value of c is nevertheless constrained by the fact that u must remain finite as $t \to 0$. The only value that satisfies this constraint is $c = 0$, and setting $c = 0$ reduces the solution to

$$\overline{u} = -\frac{1}{2}Gt + J. \tag{B10}$$

This solution does not apply at $t = 0$, but it applies for all subsequent times until runup reaches its maximum height.

Runup reaches its maximum height, H, when the head's momentum is fully depleted, in which case $\overline{u} = 0$ applies. This condition develops at $t = t_{\mathrm{stop}}$, and setting $\overline{u} = 0$ in (B10) shows that

$$t_{\mathrm{stop}} = \frac{2J}{G} = \frac{2u_0}{g}\left[\frac{1 + \frac{\kappa}{2}\frac{\rho}{\rho_0}\frac{1}{\mathrm{Fr}_0^2}\cos^3\theta}{\sin\theta + \cos\theta\tan\phi_e}\right], \tag{B11}$$

where $\mathrm{Fr}_0 = u_0/\sqrt{gh_0}$. The length of the head during maximum runup, L_{max}, is determined by integrating (B10) from $t = 0$ to $t = t_{\mathrm{stop}}$ to find that

$$L_{\mathrm{max}} = \int_0^{t_{\mathrm{stop}}} u\,\mathrm{d}t = \int_0^{2J/G}\left(-\frac{1}{2}Gt + J\right)\mathrm{d}t = \frac{J^2}{G}. \tag{B12}$$

The maximum vertical runup height is given by $H = L_{\mathrm{max}}\sin\theta$ (Figure 2c). By substituting (B8) and (B9) into (B12), this equation for H can be written in the explicit form

$$H = \frac{\left(u_0 + \frac{\kappa}{2}\frac{\rho}{\rho_0}\frac{gh_0}{u_0}\cos^3\theta\right)^2}{g\left(1 + \frac{\tan\phi_e}{\tan\theta}\right)}, \tag{B13}$$

which is easily manipulated to obtain the normalized runup formula (4) in the main text.

Equation (B13) has the desirable traits of mathematical simplicity and physical transparency, but it also has inherent limitations. First, it considers net forces acting on the entire flow head and does not account for internal force variations due to momentum transfer within the head. Second, it utilizes a constant effective basal friction angle ϕ_e that does not account for temporally or spatially varying effects of basal pore fluid pressure. Third, it does not account for locally enhanced friction caused by increased apparent weight due to the action of centrifugal forces at the foot of the adverse slope.

Acknowledgments

We thank Richard LaHusen, Jon Major, Tony Bequette, Kelly Swinford, Winston Stokes, Gordon Stratford, Dan Turner, and Carl Zimmerman for assistance with performing runup experiments at the USGS debris flow flume in 1994 and 1997. We thank reviewers Jim McElwaine, Jason Kean, Brian McArdell, and an anonymous referee, whose comments helped improve the manuscript. The data newly reported in this paper are available either as part of the supporting information or in the USGS ScienceBase data archive (doi:10.5066/F7JH3JB0). The previously published data utilized in this paper are available at the AGU FTP site noted in the paper by *Iverson et al*. [2010]: ftp://ftp.agu.org/apend/jf/2009jf001514.

References

Allstadt, K. (2013), Extracting source characteristics and dynamics of the August 2010 Mount Meager landslide from broadband seismograms, *J. Geophys. Res. Earth Surf.*, *118*, 1472–1490, doi:10.1002/jgrf.20110.

Armanini, A., M. Larcher, and M. Odorizzi (2011), Dynamic impact of a debris flow front against a vertical wall, in *Fifth International Conference on Debris-flow Hazards Mitigation, Mechanics, Prediction and Assessment*, *Italian Journal of Engineering Geology and Environment*, edited by R. Genvois, D. L. Hamilton, and A. Prestininzi, pp. 1041–1049, Casa Editrice Universita La Sapienza, Rome, doi:10.4408/IJEGE.2011-03.B-113.

Choi, C. E., S. C. H. Au-Yeung, C. W. W. Ng, and D. Song (2015), Flume investigation of landslide granular debris and water runup mechanisms, *Géotech. Lett.*, *5*, 28–32.

Chu, T., D. M. McClung, R. Ngun, and R. Sherkat (1995), Experiments on granular flows to predict avalanche runup, *Can. Geotech. J.*, *32*, 285–295.

George, D. L. (2010), Adaptive finite volume methods with well-balanced Riemann solvers for modeling floods in rugged terrain: Application to the Malpasset dam-break flood (France, 1959), *Int. J. Numer. Meth. Fluids*, doi:10.1002/fld.2298.

George, D. L., and R. M. Iverson (2014), A depth-averaged debris-flow model that includes the effects of evolving dilatancy. II. numerical predictions and experimental tests, *Proc. R. Soc. Lond. Ser. A*, *470*, doi:10.1098/rspa.2013.0820.

Guthrie, R. H., P. Friele, K. Allstadt, N. Roberts, S. G. Evans, K. B. Delaney, D. Roche, J. J. Clague, and M. Jakob (2012), The 6 August 2010 Mount Meager rock slide-debris flow, Coast Mountains, British Columbia: Characteristics, dynamics, and implications for hazard and risk assessment, *Nat. Hazards Earth Syst. Sci.*, *12*, 1277–1294, doi:10.5194/nhess-12-1277-2012.

Hákonardóttir, K. M., A. Hogg, and T. Jóhannesson (2003), A laboratory study of the interaction between supercritical, shallow flows and dams, Icelandic Meteorological Office (Vedurstofa Islands) Report 03038.

Hungr, O., and D. H. McClung (1987), An equation for calculating snow avalanche runup against barriers, in *Proceedings of the 1986 Davos Symposium of Avalanche formation, Movement, and Effects*, *IAHS Publication*, vol. 162, pp. 605–612.

Hungr, O., G. C. Morgan, and R. Kellerhals (1984), Quantitative analysis of debris torrent hazards for design of remedial measures, *Can. Geotech. J.*, *21*, 663–677.

Hungr, O., G. C. Morgan, D. F. VanDine, and D. R. Lister (1987), Debris flow defenses in British Columbia, in *Debris flows/Avalanches: Process, Recognition, and Mitigation*, *Geol. Soc. Am. Rev. Eng. Geol.*, vol. 7, edited by J. E. Costa and G. F. Wieczorek, pp. 201–222.

Iverson, R. M. (1997), The physics of debris flows, *Rev. Geophys.*, *35*, 245–296, doi:10.1029/97RG00426.

Iverson, R. M., and R. P. Denlinger (2001), Flow of variably fluidized granular masses across three-dimensional terrain: 1. Coulomb mixture theory, *J. Geophys. Res.*, *106*(B1), 537–552, doi:10.1029/2000JB900329.

Iverson, R. M., and D. L. George (2014), A depth-averaged debris-flow model that includes the effects of evolving dilatancy. I. physical basis, *Proc. R. Soc. Lond. Ser. A*, *470*, 20130819, doi:10.1098/rspa.2013.0819.

Iverson, R. M., and D. L. George (2016), Modeling landslide liquefaction, mobility bifurcation, and the dynamics of the 2014 Oso disaster, *Geotechnique*, *66*, 175–187, doi:10.1680/jgeot.15.LM.004.

Iverson, R. M., M. Logan, R. G. LaHusen, and M. Berti (2010), The perfect debris flow? Aggregated results from 28 large-scale experiments, *J. Geophys. Res.*, *115*, F03005, doi:10.1029/2009JF001514.

Jibson, R. W., E. L. Harp, W. Schulz, and D. K. Keefer (2006), Large rock avalanches triggered by the **M** 7.9 Denali Fault, Alaska, earthquake of 3 November 2002, *Eng. Geol.*, *83*, 144–160, doi:10.1016/j.enggeo.2005.06.029.

Jóhannesson, T., P. Gauer, P. Issler, and K. Lied (Eds.) (2009), *The Design of Avalanche Protection Dams, Project Report EUR 23339*, European Commission Directorate for Research, Brussells.

Johnson, C. G., B. P. Kokelaar, R. M. Iverson, M. Logan, R. G. LaHusen, and J. M. N. T. Gray (2012), Grain-size segregation and levee formation in geophysical mass flows, *J. Geophys. Res.*, *117*, F01032, doi:10.1029/2011JF002185.

Logan, M., and R. M. Iverson (2007), Video documentation of experiments at the USGS debris-flow flume, 1992–2006 (amended to include 2007–2013), *U.S. Geol. Sur. Open-file Rept. 2007-1315* (DVD set and posted online at. [Available at http://pubs.usgs.gov/of/2007/1315/.]

Loughlin, S. C., E. S. Calder, A. Clarke, P. D. Cole, R. Luckett, M. T. Mangan, D. M. Pyle, R. S. J. Sparks, B. Voight, and R. B. Watts (2002), Pyroclastic flows and surges generated by the 25 June 1997 dome collapse, Soufriére Hills Volcano, Montserrat, in *The Eruption of Soufriére Hills Volcano, Montserrat, from 1995 to 1999*, *Geol. Soc. Lond. Mem.*, vol. 21, edited by T. H. Druitt and B. P. Kokelaar, pp. 191–209.

Major, J. J., and R. M. Iverson (1999), Debris-flow deposition—Effects of pore-fluid pressure and friction concentrated at flow margins, *Geol. Soc. Am. Bull.*, *111*, 1424–1434.

Mancarella, D., and O. Hungr (2010), Analysis of run-up of granular avalanches against steep, adverse slopes and protective barrier, *Can. Geotech. J.*, *47*, 827–841.

Pierson, T. C. (1985), Initiation and flow behavior of the 1980 Pine Creek and Muddy river lahars, Mount St. Helens, Washington, *Geol. Soc. Am. Bull.*, *96*, 1056–1069, doi:10.1130/0016-7606.

Savage, S. B., and K. Hutter (1989), The motion of a finite mass of granular material down a rough incline, *J. Fluid Mech.*, *199*, 177–215.

Takahashi, T., and H. Yoshida (1979), Study on the deposition of debris flows, Part 1—Deposition due to abrupt change of the bed slope [in Japanese with English abstract], *Annals of the Disaster Prevention Research Institute*, Kyoto Univ., Japan, 22 B-2.

Zanuttigh, B., and A. Lamberti (2007), Instability and surge development in debris flows, *Rev. Geophys.*, *45*, RG3006, doi:10.1029/2005RG000175.